Department of Physics and Astronomy
Heidelberg University

Bachelor Thesis in Physics
submitted by

Henry Rainer

born in Mannheim (Germany)

2024

Air cooling tests for the Outer Tracker detector of ALICE 3

This Bachelor Thesis has been carried out by Henry Rainer at the
Physikalisches Institut in Heidelberg
under the supervision of
Prof. Dr. Johanna Stachel

Abstract

The ALICE 3 project represents a significant advancement in detector technology, aiming to succeed the current ALICE 2 detector at the Large Hadron Collider (LHC). It will feature a unique all silicon tracking detector capable of unprecedented pointing resolution and material budget.
This thesis investigates the feasibility of employing air cooling systems for the outer tracker detector of ALICE 3. Through a series of experimental studies, various cooling strategies and input conditions were examined, with results compared against theoretical model predictions and computational fluid dynamics (CFD) simulations conducted using the COMSOL Multiphysics platform. The primary objective was to establish a comprehensive model to predict the requirements and parameters necessary for effective air cooling to maintain the desired temperature levels within the outer tracking detector under designated operational conditions.
The thesis contributes to the ongoing development of the ALICE 3 detector by providing valuable insights into the practical implementation of air cooling solutions for critical components. The results presented herein not only validate the feasibility of air cooling but also offer a deeper understanding of thermodynamics, fluid dynamics and its applications.

Zusammenfassung

Das ALICE 3 Projekt stellt einen signifikanten Fortschritt in der Detektortechnologie dar und wird den aktuellen ALICE 2 Detektor am Large Hadron Collider (LHC) ablösen. Es beinhaltet einen einzigartigen Tracking-Detektor, der komplett auf Silizium Technologie basiert und eine beispiellose Auflösung sowie Materialbudget haben wird.
Diese Arbeit untersucht die Realisierbarkeit der Verwendung von Luftkühlungssystemen für Teile des Outer-Tracker Detektor von ALICE 3. Mithilfe einer Serie an Experimenten wurden verschiedene Kühlungsstrategien und Konditionen getestet. Die Ergebnisse wurden mit theoretischen Rechnungen sowie Simulationen mit numerischer Strömungsmechanik (CFD) mittels der COSMOL Multiphysics Software verglichen und ausgewertet. Das Hauptziel dieser Arbeit bestand darin, ein umfassendes Modell zur Vorhersage für die Anforderungen und nötigen Parameter zur effektiven Luftkühlung des Outer-Tracking Detektors unter festgelegten betrieblichen Bedingungen zu erstellen.
Diese Arbeit trägt durch die Bereitstellung wertvoller Einblicke in die praktische Implementierung von Luftkühlung kritischer Komponenten zur fortlaufenden Entwicklung des ALICE 3 Detektors bei. Die in dieser Arbeit vorliegenden Ergebnisse bestätigen die Realisierbarkeit der Luftkühlung und bieten zudem einen tieferen Einblick in die Bereiche der Thermodynamik und Strömungsmechanik sowie deren Anwendungen.

Contents

1   ALICE 3

In this chapter I will give a brief overview of the LHC and ALICE facilities and introduce the proposed ALICE 3 detector with its expected benefits over the present version. Finally I will describe the Outer Tracker of ALICE 3 with its cooling requirements to set the conditions on the setup of the air cooling experiments conducted in this thesis.

1.1   ALICE and the LHC

The Large Hadron Collider (LHC) is currently the worlds largest particle accelerator consisting of a 27-kilometre ring of superconducting electromagnets located at the European Center for Nuclear Research (CERN) near Geneva [14]. Particles travel at ultra relativistic speeds and collide at four major particle detectors. These include two general-purpose detectors, namely A Toroidal LHC Apparatus (ATLAS) and Compact Muon Solenoid (CMS) alongside the Large Hadron Collider beauty (LHCb), which study differences between matter and antimatter with focus on bottom (or beauty) quarks.

The fourth detector is called A Large Ion Collider Experiment (ALICE) which studies heavy-ion physics, specifically the quark-gluon plasma (QGP) which is the subject of Quantum chromodynamics (QCD)[6].
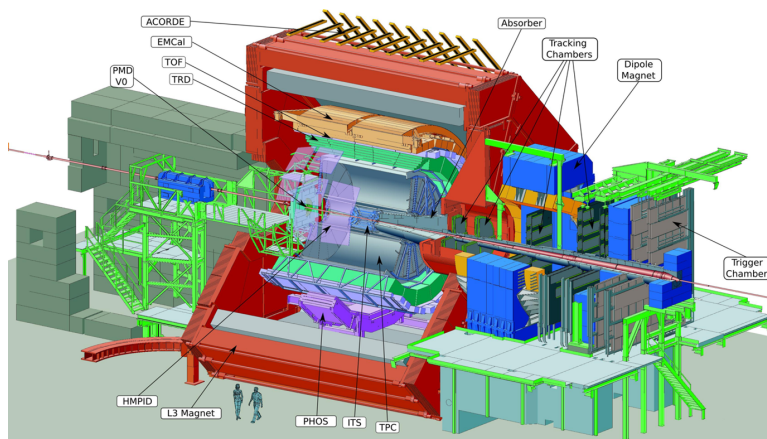

Figure 1: Overview of the present ALICE detector systems [2]

For the study of the QGP in laboratory conditions, heavy-ion collisions (Pb-Pb) are utilized as model system. Collisions with lighter ions (Xe-Xe, O-O) are also

included for lower energy running as well as interaction volume variation. ALICE also takes data with proton-proton (pp) collisions for reference data collection. The ALICE detector measures 16 m x 16 m x 23 m, has a total weight of approximately 10000 t and features 18 different detector systems.

1.2 ALICE 3

After an upgrade of the detector to ALICE 2 for LHC Run 3 fundamental questions remain open, even after Run 4, like the hadronisation mechanisms of the medium, the partonic equation of state and its temperature dependence as well as the underlying dynamics of chiral symmetry restoration. Therefore, further precision differential measurements of dileptons, systematic measurements of heavy-flavoured hadrons and hadron interactions are needed. This is where ALICE 3 comes into play. The following figure shows a proposed sketch of the ALICE 3 detector which depicts all its key elements.
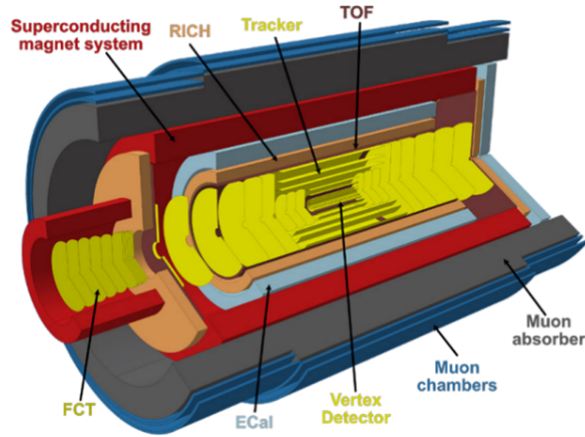
Figure 2: Conceptual overview of the ALICE 3 detectors [4]

The tracking detector is completely based on silicon technology which has many benefits, including a much lower mass material budget, which will be a big change to the current state. The tracker is comprised of 11 barrel layers and 12 forward discs on each side. The barrel is divided into the Vertex detector, featuring the first 3 layers and discs and the Outer Tracker. In contrast to the current tracking detector the Vertex Detector is mounted inside the beam pipe, with the first layer with only a 5 mm radius around the beam pipe, therefore providing a

substantially improved pointing resolution (see figure 1.2). Those improvements will enable heavy flavour hadron detection with very high purity and efficiency, which enables measurements of processes with a direct access to heavy quark interactions with the quark–gluon plasma [4].

The following detectors are Time-Of-Flight (TOF), ring-imaging-Cherenkov (RICH), calorimeters (ECal) and forward-conversion-trackers (FCT). Up to a few GeV/c, $e^{\pm}/\pi^{\pm}$ separation will be provided with the TOF detectors. This is due to the silicon sensors which have an extremely high timing resolution of roughly 20 ps. The RICH detectors will use aerogel as radiator material, giving additional particle identification capabilities.

The overall improvement of each individual detector and component will give better results and a more complete understanding regarding microscopic dynamics of the strongly-interacting matter produced in heavy-ion collisions.
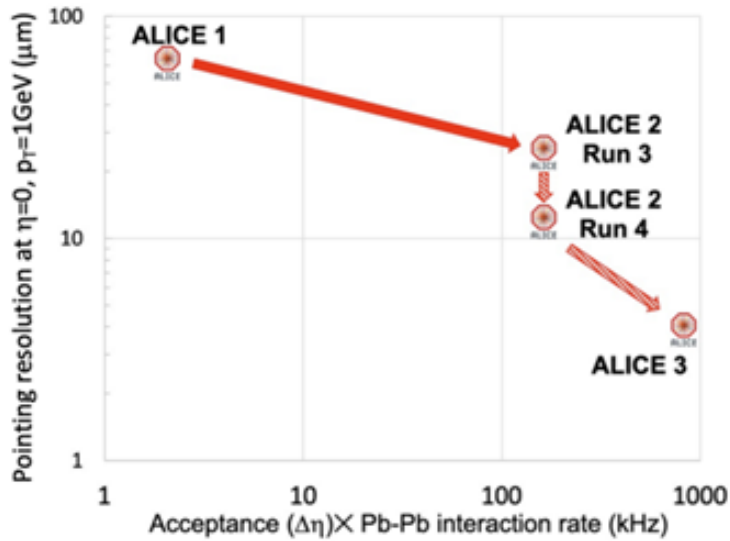

Figure 3: Pointing resolution and effective expected statistics in heavy-ion collisions for ALICE 1, 2, 2.1 and 3 [5]

1.2.1 Outer Tracking System of ALICE 3

The Outer Tracker is comprised of the outer 8 barrel layers and 2x9 forward disks. Here is an overview over its geometry and dimensions.
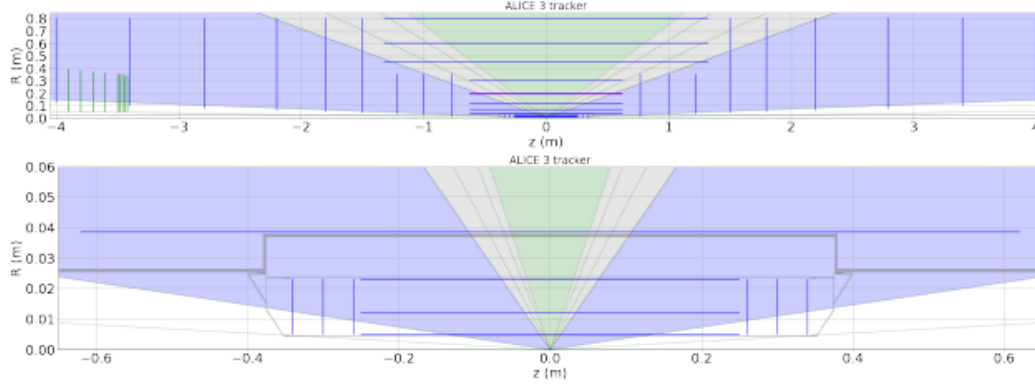
Figure 4: Schematic R-z view of the full tracker (top) and of the vertex detector separately (bottom). The blue lines represent the tracking layers. The FCT disks are marked in green. The beampipe corresponds to R = 0. [4]

Layer	Material thickness ($\%X_0$)	Intrinsic resolution (μm)	Barrel layers		Forward discs		
			Length ($\pm z$) (cm)	Radius (r) (cm)	Position ($|z|$) (cm)	R_{in} (cm)	R_{out} (cm)
0	0.1	2.5	50	0.50	26	0.50	3
1	0.1	2.5	50	1.20	30	0.50	3
2	0.1	2.5	50	2.50	34	0.50	3
3	1	10	124	3.75	77	5	35
4	1	10	124	7	100	5	35
5	1	10	124	12	122	5	35
6	1	10	124	20	150	5	80
7	1	10	124	30	180	5	80
8	1	10	264	45	220	5	80
9	1	10	264	60	279	5	80
10	1	10	264	80	340	5	80
11	1				400	5	80

Figure 5: Geometry and key specifications of the tracker [4]

The barrels themselves are comprised of staves with the mounted detector modules arranged in an overlapping structure around the axis. CMOS Monolithic Active Pixel Sensors (MAPS) is the choice of technology for the detector. For the barrel layers 3-7, which have a total length of 124 cm, water cooling is foreseen with using a leakless cooling system. This thesis is focused on the the three outer layers 8-10 and investigates whether air cooling is sufficient for them. These barrels have a total length of 264 cm but will be split in the middle to feature a support structure for mechanical reasons. This means that a possible air cooling access could be laid

there as well. That amounts to a total length of 132 cm of the individual staves, for which we need to find a cooling solution. As further explained in chapter 3.1, a single stave of the barrel with 130 cm length will be used for the air cooling tests.
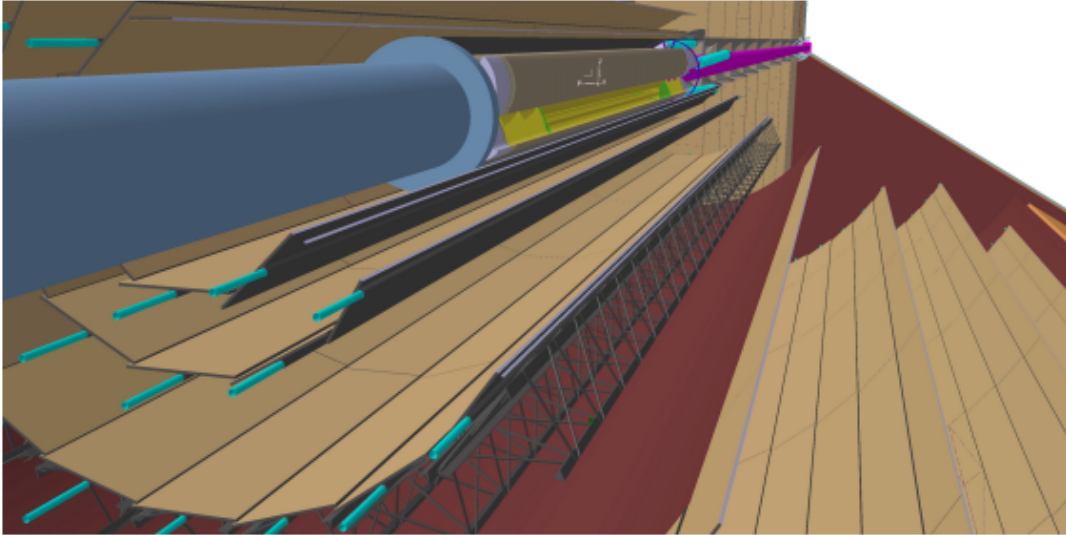

Figure 6: Sketch of the outer tracker mechanics. Modules assembled in stave structures are visible as well as services and cooling pipes. Furthermore, the overlap of the staves can be seen. [4]

The smallest distance between barrel layers of the outer 3 barrels is 15 cm (distance between 7-8 and 8-9). This sets the conditions on the width of the air duct used. Since the air duct used in the following experiments is a tube while the real duct between the barrels has more similarities to a flow between two endless planes, which is a difference in geometry - I will touch on this topic in chapter 2.1 when discussing characteristic lengths.

Another important characteristic of the outer tracker is its power consumption, since the power density [W/m²] will need to be accounted for as heat flux with the cooling measures. For the outer tracker a maximum power density of 30 mW/cm² is expected. This is, however, only a target number, since the chip technology for the detector boards is not fully developed yet.
30 mW/cm² or 300 W/m² is the approximate standard power density chosen in the following experiments. Since a significant amount of this heat flux is simply

emitted via radiation in the cooling tests described in this work, which is not the case in the final ALICE 3 detector, and also the power density of the detector is not certain yet, the results of the experiments (conducted with 300 W/m^2) should not be taken as a definite approximation of the actual temperatures. Instead with varying different inputs of the experiments we will try to establish a connection to theoretical predictions of the model, which will enable us to predict the cooling performance of the real application once the final input conditions (such as air temperature, air volumetric flow and power density) are known.

2 Theory of heat transfer

This chapter is mostly based on the book [3]. There are three fundamental modes of heat transfer: conduction, convection and radiation.

Conduction describes the heat transfer within an object by diffusion. Energy diffuses, caused by the interaction of moving molecules, atoms and electrons. It is characterized by the thermal conductivity k of the object, within Fouriers law, where q is the heat flux [W/m^2]:

$$q = -k * \frac{dT}{dx} \qquad (1)$$

We can use this law to describe the heat transfer within the detector plates (in this experiment the PCBs described in 3.1).
Convection is defined as heat transfer between a solid surface and a surrounding fluid. It really has two components: conduction (within the fluid) and advection, which is heat transfer by bulk fluid flow. Convection is characterized by the convective heat transfer coefficient h which is part in Newtons law of cooling:

$$q = h * (T_s - T_\infty) \qquad (2)$$

T_s is the surface temperature and T_∞ is the free stream fluid temperature. Since h is not a material property like k, finding a local or average h is the challenge when analyzing convective heat transfer. Convection is the defining process of the application in this thesis.
The last mode of heat transfer is radiation, which is described by the Stefan-Boltzmann law:

$$q = \sigma * T^4 \qquad (3)$$

σ is the Stefan-Boltzmann constant.

2.1 Convection

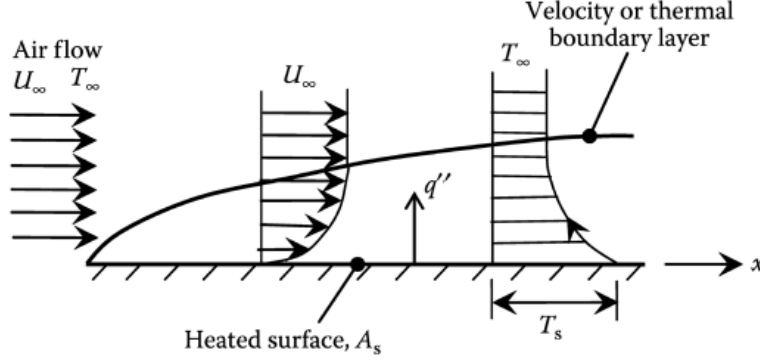Let us introduce the concept of boundary layers:

Figure 7: Velocity and thermal boundary layer [3]

When a flow with uniform temperature and velocity hits a surface, a temperature and velocity gradient starts to form along this surface. The velocity boundary layer thickness δ is then defined as the y distance from the surface, at which the velocity $u(y)$ is 99% of the free stream velocity u_∞:

$$\frac{u(y)}{u_\infty} = 0.99 \rightarrow \delta = y \qquad (4)$$

The same goes for the thermal boundary layer thickness δ_T:

$$\frac{T_s - T(y)}{T_s - T_\infty} = 0.99 \rightarrow \delta_T = y \qquad (5)$$

At the surface (y=0) we can then equate 1 and 2 to get:

$$h = \frac{-k_f(\partial T/\partial y)\,|_{y=0}}{T_s - T_\infty} \qquad (6)$$

k_f is the thermal conductivity of the fluid. We further need to introduce three important dimensionless variables.

The Reynolds number Re is a measure of the turbulence of a fluid flow with density ρ, characteristic length scale L, velocity u and dynamic viscosity μ. It can also be written in terms of the kinematic viscosity $\nu = \mu/\rho$, which is also known as the momentum diffusivity.

$$Re = \frac{\rho u L}{\mu} = \frac{uL}{\nu} \qquad (7)$$

8

The characteristic length L is a scale defining dimension of the geometry of the model, for pipe flow it is best approximated as the pipe diameter d, for flow over a flat plate its best approximation is the (variable) distance x down the plate. For flow between two endless plates it is approximated as double their distance: in chapter 1.2.1 where we named the smallest distance between barrel layers as 15 cm, we would get a characteristic length of 30 cm, which is larger then the characteristic length of our tube (24 cm), which means we will not overestimate the air space and therefore cooling performance in that regard.

We further introduce the Prandtl number Pr, which indicates the relation between momentum diffusivity and thermal diffusivity α and is also related to the relation of the Velocity/ thermal boundary layers δ and δ_T. It is property of the fluid with specific heat capacity c_p.

$$Pr = \frac{c_p \mu}{k} = \frac{\nu}{\alpha} \sim \frac{\delta}{\delta_T} \tag{8}$$

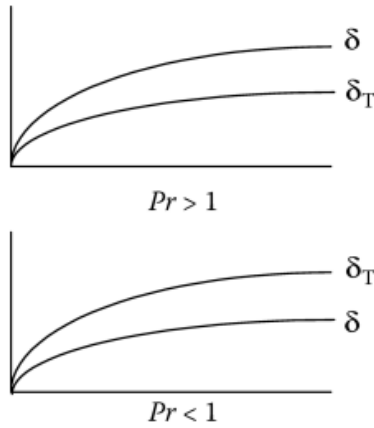Figure 8: Boundary layers: relation to Prandtl number, the axes are x- and y-length of the flow [3]

The last dimensionless variable and the one we will want to solve for is the Nusselt number Nu. It is the ratio of convective to conductive heat transfer and is generally a function of Reynolds and Prandtl number. L and k are again characteristics of the fluid:

$$Nu = \frac{hL}{k} = a * Re^b * Pr^c \tag{9}$$

Finding this relation (a,b and c) allows us then to back solve for h. This is done by solving the following three equations simultaneously inside the boundary layers. Conservation of mass:

$$\frac{\partial \rho}{\partial t} + \vec{\nabla} * (\rho \vec{V}) = 0 \tag{10}$$

Conservation of momentum (p being pressure and g gravitational acceleration):

$$\rho \frac{d\vec{u}}{dt} = -\vec{\nabla}p + \mu \vec{\nabla}^2 \vec{u} + \rho \vec{g} \tag{11}$$

Conservation of energy:

$$\rho \frac{dh}{dt} = \frac{dp}{dt} + \vec{\nabla} * k \vec{\nabla} T + \mu \Phi + \dot{q} \tag{12}$$

Here $\dot{q}$ is the heat generation per volume [W/m³] and $h = e + (1/2)\vec{u}^2$, where e is the specific internal energy. Φ is the dissipation function:

$$\Phi = 2\left[\left(\frac{\partial u_x}{\partial x}\right)^2 + \left(\frac{\partial u_y}{\partial y}\right)^2 + \left(\frac{\partial u_z}{\partial z}\right)^2\right] + \left(\frac{\partial u_x}{\partial y} + \frac{\partial u_y}{\partial x}\right)^2 + \left(\frac{\partial u_x}{\partial z} + \frac{\partial u_z}{\partial x}\right)^2 + \left(\frac{\partial u_z}{\partial y} + \frac{\partial u_y}{\partial z}\right)^2 \tag{13}$$

Those equations can only be solved analytically for special cases, such as for example laminar flow over a flat plate. Doing so is a quite elaborate task and not in the scope of this thesis. Further information on this can be found in chapters six and seven of [3].

The alternative is to solve the problem numerically with a simulation software, which we will do in chapter 5.

2.1.1 Turbulent heat transfer

The critical Reynolds number Re_C is the Reynolds number at around which the flow transitions from a laminar into a turbulent regime. It is approximated as ~2300 for flow in a pipe and ~500,000 for flow over a flat plate and is also strongly dependent on surface roughness.

As the flow transitions into the turbulent regime unsteady vortices appear in the flow. The velocity profile is now best described as having an average velocity part plus a time varying velocity. I will pick up on this in chapter 5.1.
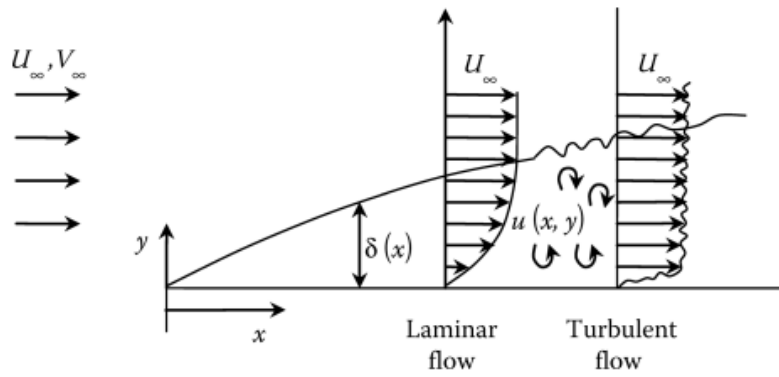
Figure 9: Typical turbulent boundary-layer flow velocity and temperature profile [3]

This causes turbulent mixing of the fluid, which increases the heat transfer. Also the boundary layer strongly increases, which on the other hand reduces heat transfer. Generally speaking, turbulence enhances heat transfer.
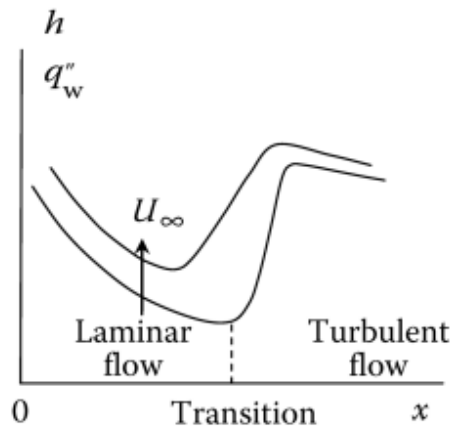
Figure 10: Heat transfer coefficient and heat flux profile [3]

In addition to analytical models, it is common to use empirical relations from experiments to find a relation between Nusselt, Prandtl and Reynolds number. In [3] (chapter 10.3) a theoretical model for turbulent fully developed pipe flow is derived, which is close to the following empirical correlation, which we will try to apply to our experiment.

$$Nu = 0.023 Re^{0.8} Pr^{0.4} \tag{14}$$

2.1.2 Internal convection

Internal convection describes convection due to fluid flow around surfaces, which make up a confined space, such as in a pipe or between plates. The boundary layers from each side grow towards another, once they join a static temperature and velocity profile emerges - this is then called fully developed flow.
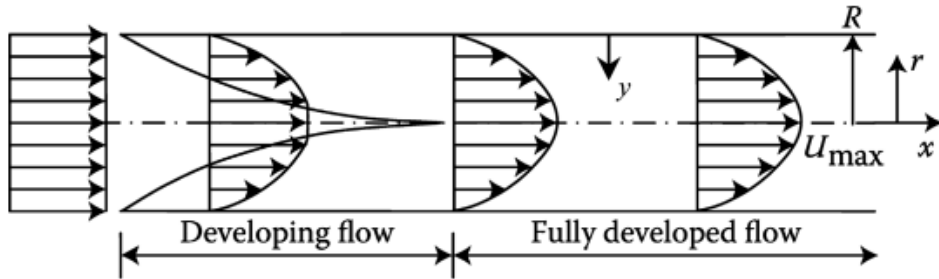
Figure 11: Velocity profile distribution in a circular tube or between two parallel plates [3]

The length down the flow from entrance to the intersection of the boundary layers, is called the entrance length. There is a hydrodynamic entrance length X and a thermal entrance length X_T. For laminar flow they are approximated as:

$$\frac{X}{L} \approx 0.05 Re \tag{15}$$

$$\frac{X_T}{L} \approx 0.05 Re \tag{16}$$

with L being the characteristic length. And for turbulent flow as:

$$\frac{X}{L} \approx 10 \tag{17}$$

$$\frac{X_T}{L} \approx 10 \tag{18}$$

However it has to be noted that those approximations, especially for turbulent can vary strongly with different geometries.

For a constant surface flux q_s and a fixed cross-section (pipe), the bulk mean

temperature T_b gradient is constant. With a mass flow rate $\dot{m}$ a heated area A and an initial fluid temperature T_i we get:

$$q_s = \frac{\dot{m}c_P}{A}\frac{dT_b}{dx} \qquad (19)$$

$$T_b = T_i + \frac{q_s A}{\dot{m}c_P} * x \qquad (20)$$

In the fully developed region, where the temperature profile and heat transfer coefficient are constant, this then also applies to the surface temperature.
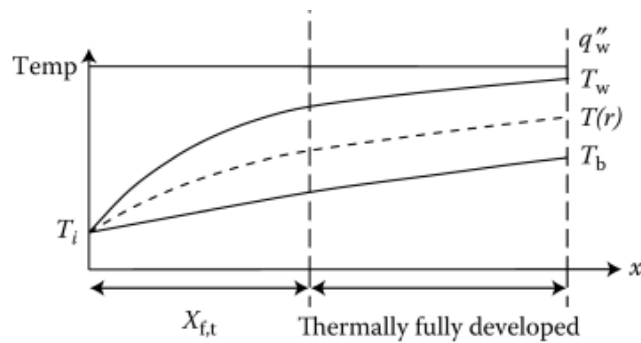

Figure 12: Laminar flow in a circular tube with the uniform surface heat flux: temperature profile, T_W is the surface temperature [3]
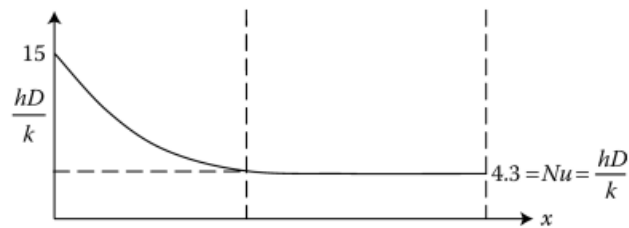

Figure 13: Laminar flow in a circular tube with the uniform surface heat flux: heat transfer coefficient [3]

13

3 Air cooling

The objective in this thesis is to test the general feasibility and performance of air cooling methods for the three outer barrel layers of the outer tracker of ALICE 3. The general idea behind air cooling as opposed to water cooling, which is the realized method of the current detector is the following. Because water cooling needs the implementation of cold plates and a leakless cooling system inside the detector, it has two major disadvantages. Having extra material inside the detector means having a larger material budget, which worsens detector performance. Second, building the support structure of the water cooling system is arguably more expensive than a simple air supply.

This section contains the description and results of the simulating experiments. The order in which the experiments are presented is the same order as in which they were carried out (30.01.24 - 20.02.24). Constants and material properties used in calculations are all taken from [16].

Since it is impossible to properly estimate the actual differences of cooling performance between the simulating experiments and a real life implementation, I will not include any estimations of error margins in the discussions. Many discussions will be purely qualitative and quantitative discussions will be limited to differences between the experimental setups.

3.1   General experiment setup

As introduced in chapter 1.2.1 the barrel layers of the outer tracker are made up of staves with the detector modules mounted on top of them. To simulate the detector modules, ten PCBs (printed circuit board) per stave are used, which are described in the following.

A single PCB has a length of 130 mm, width of 80 mm and thickness of 0.8 mm. It is comprised of the material FR-4 plus two layers of copper of the thickness 35 μm. The bottom layer is etched to connect twelve onboard temperature sensors and four air temperature sensors, which are mounted on the bottom side. The sensors have an error margin of 0.1 °C according to specifications. On all PCBs used only one of the four possible air sensors is equipped, with the exception of the one on the far left side (left in the sense of all future setups and resulting plots), where all four are equipped. The air sensors are connected via wire to the PCB and their position can be manually changed.
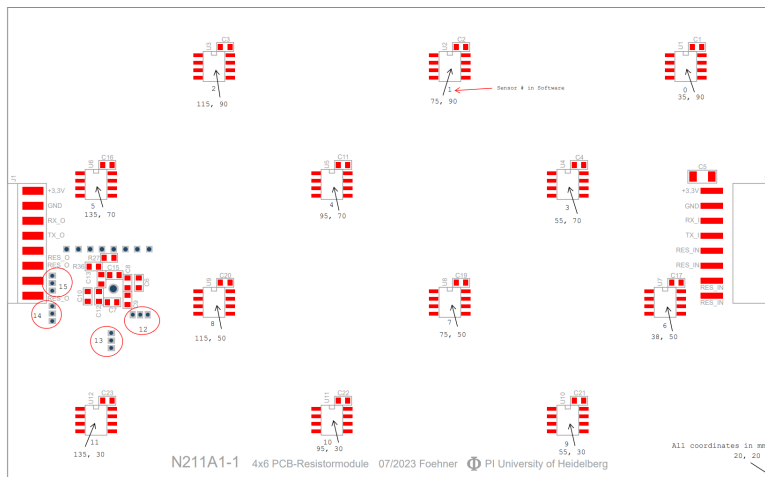
Figure 14: Bottom side of the PCB: positions of the onboard temperature sensors [18]

As one can see there are four rows of onboard temperature sensors with three sensors per PCB. Their y-positions are 10 mm, 30 mm, 50 mm and 70 mm. In the following analyses of the experiments those four rows will be plotted as four line plots to present static temperature distributions.

The layer on the top side is etched in a way to provide heating resistance plus a small area featuring the FPGA (Field Programmable Gate Array), which handles

the signals of the temperature sensors. To make up for the missing heating coils in the position of the FPGA, resistors with equal resistance to their area are mounted. 5mm on each side of the PCB do not contain the heating coils and therefore cannot produce any heat.
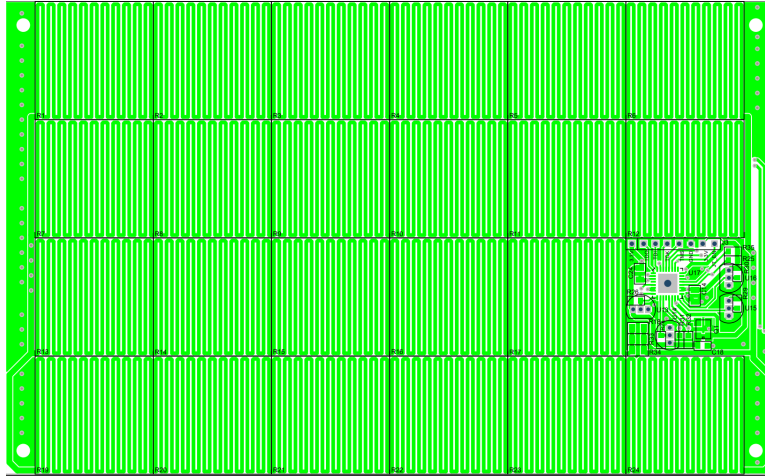
Figure 15: Top side of the PCB: etched heating coils and the FPGA on the right hand side[18]

The ten PCBs are coupled in series with the heating circuit being connected to a power supply and the temperature sensor circuit being linked to the server via USB. The PCBs are screwed on small bases which are glued to the large space frame (stave).
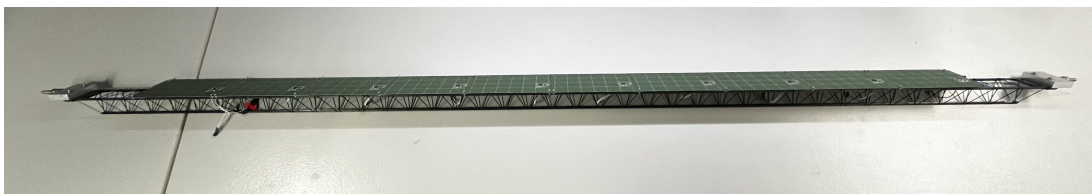
Figure 16: full construction of a stave plus the mounted PCBs

For better readability the full construction of a stave plus the ten mounted PCBs will be referred to as a "stave" in the following.

The main setup consists of a two meter long acrylic glass tube with a diameter of 25 cm (inner diameter is 24 cm), which confines the whole experiment and simulates the limited air space in the real detector. Holes (1 cm diameter) are drilled in one line at the positions 10 cm; 35 cm; 67.5 cm; 100 cm; 132.5 cm; 165

16

cm; 190 cm. This gives the option to insert a hot wire anemometer to measure air speed inside the tube. The one used has an error margin of 0.1 m/s according to specifications.

Two mounting brackets (acrylic glass) can be fit at any position in the tube and are used to hold one or more staves in the middle or displaced from the middle of the tube.

Figure 17: The acrylic glass tube
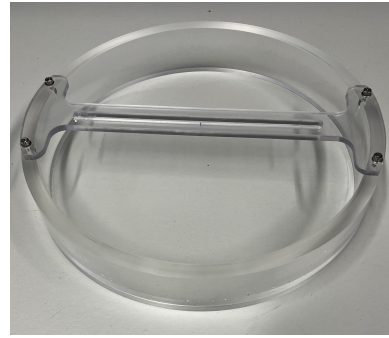
Figure 18: One of two mounting brackets

The temperature data is read out with a C++ program on the server. The program produces a file with a temperature entry for every sensor (120 total onboard plus 40 total air sensors) for every second the readout program is run. This file can directly be used to plot the temperature versus time for chosen sensors. To make static plots of a temperature distribution over the stave at a chosen time, the data has to be rewritten. I wrote a C++ program (enclosed in the appendix A) which rewrites the simple temperature file and a list of sensor coordinates into multiple different files used for different plot styles. In addition to the one shown in this thesis it is also possible to produce 3D plots (x, y and T) or an animated gif of the full temperature distribution over time. Since the line plots are the easiest to analyze, I did not include other plots then those, but I can provide them if required.

3.2 Pilot study with a single PC fan

3.2.1 Setup

To get an initial idea of how well air cooling performs in general, this experiment is conducted. The stave is mounted in the middle of the tube with the mounting brackets. A 12 V-PC fan is fit to the right end of the tube with a mounting clamp. To prevent back flow, simple plastic wrap is draped around the open space between fan and tube. The left side is left open.
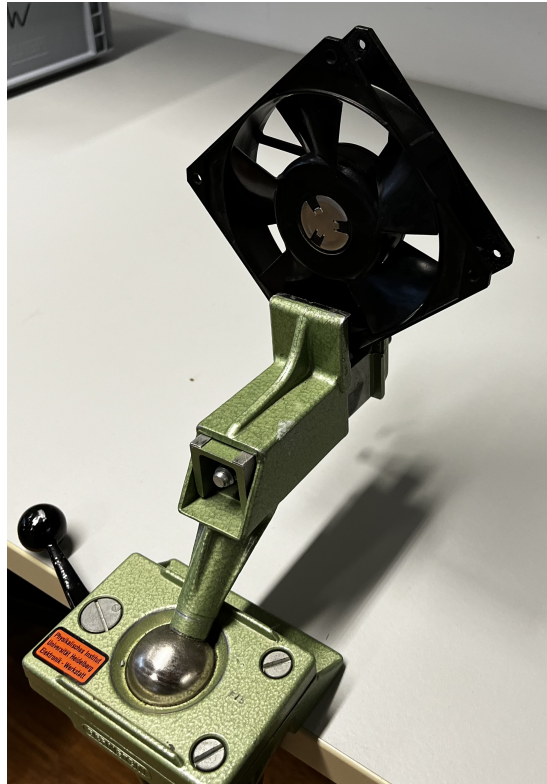
Figure 19: PC fan with mounting clamp

With the start of the experiment the fan was switched on as well as the heating power. The temperature readout ran for 600s. The room temperature was 22.6°C. The power output of the stave was 30.1 W. In this setup the anemometer was not there yet, so there is no information about the fluid speed.
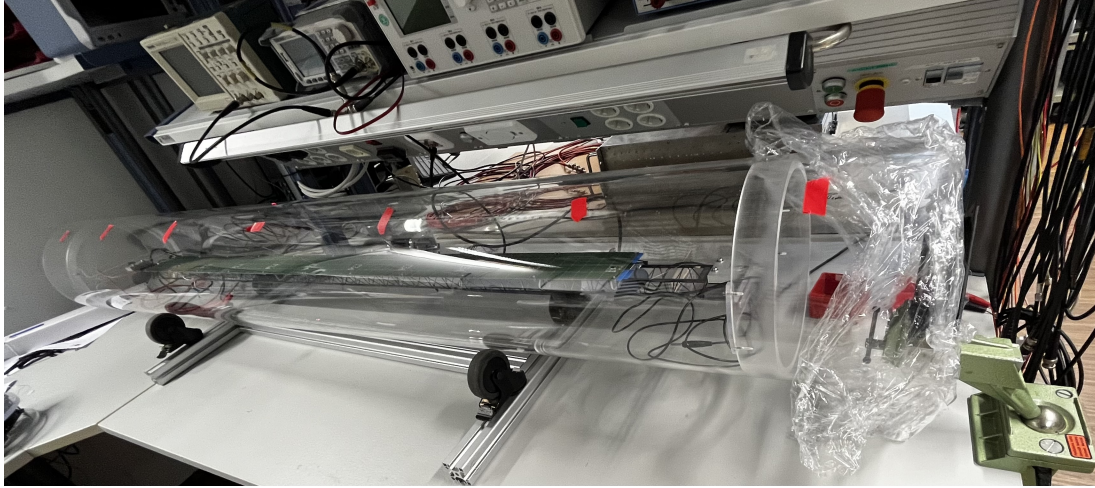
Figure 20: Complete Setup

3.2.2 Results

The first thing being noticed is that with rising temperature the heating power output slightly increases. Since the power supply for the heating is run in current limit mode (constant current), this can be explained as follows: with rising temperature the resistance of the heating coils (copper) increases, thus to keep a constant current, the voltage is increased: $U = R_{increasing} * I_{const}$. This makes for the increase in power: $P = U_{increasing} * I_{const}$. Because the increase in power is only of the order of 0.1 W this is negligible and the documented power output for this and all following experiments is given as the constant power at the final reached temperature.

Here are plots of the development of the temperature over time:

Figure 21: Temperature over time for board 10 (rightmost), every plotline represents one sensor, b for board and a for air

Figure 22: Temperature over time for board 1 (leftmost), every plotline represents one sensor, b for board and a for air

As one can see the temperature settles in about two minutes on the right side of the stave (represented by board 10) and in about four minutes on the left side of

the stave (represented by board 1), where a higher temperature is reached.

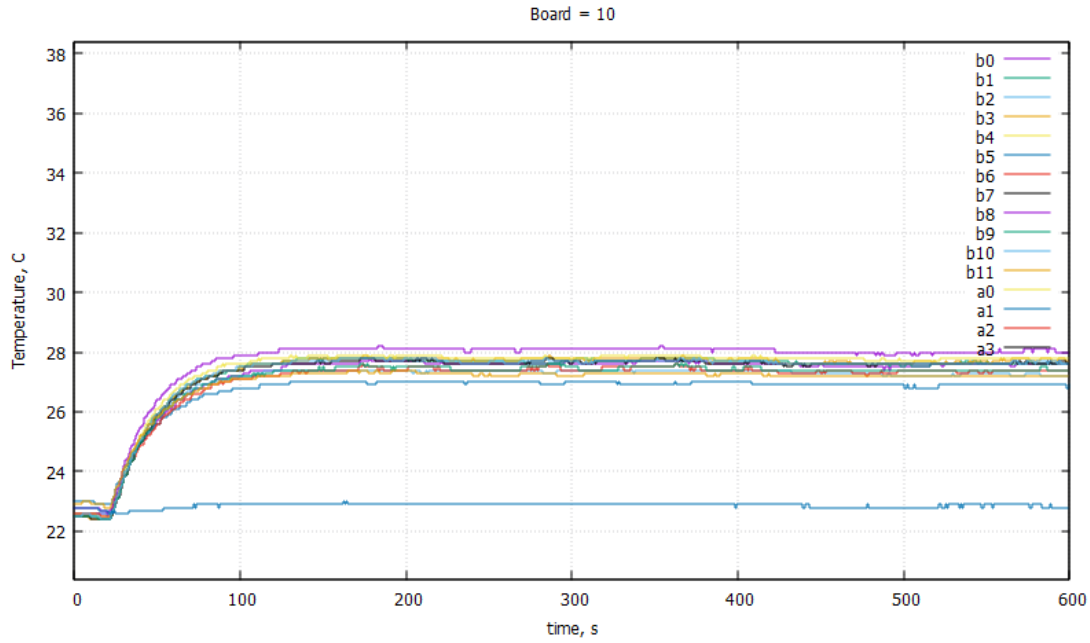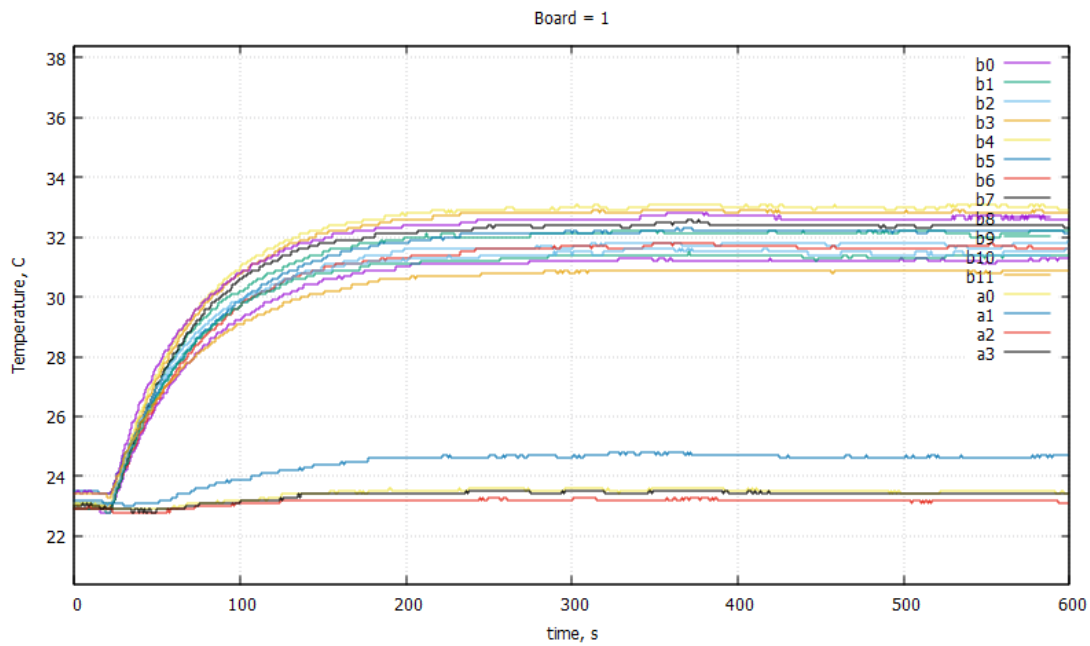Since we are mostly interested in the static temperature that settles after the "startup time" the temperature development over time is of minor importance. In the future experiments it will therefore not be discussed. The static time taken is usually the one at the ten minute mark, however in all experiments there is a temperature readout over the full time and plots like the ones above are used to make sure that the temperature is truly static.

Now for the discussion of the static temperature distribution:
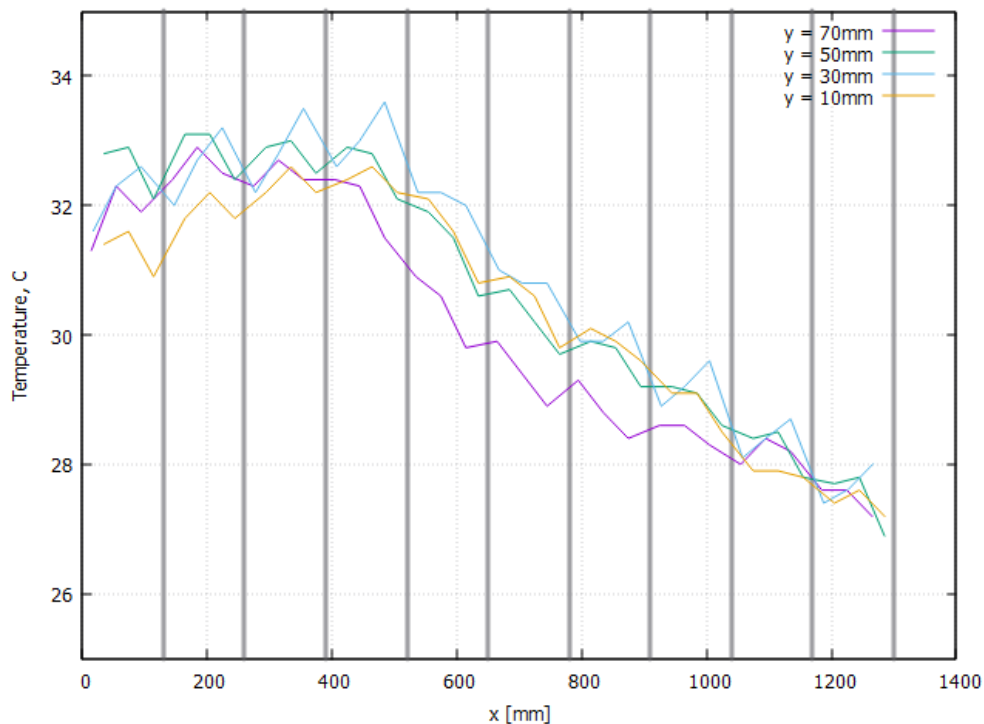
Figure 23: Temperature distribution plot of the PCB sensors at 10 min (input temp.: 22.6 °C): x-axis corresponds to the x position on the PCBs, one plotted line for each y-position on the PCBs, vertical lines to mark PCB transitions

We can see a temperature rise from about 27 °C on the right side, where air is being blown into the tube. The maximum temperature of around 33 °C is reached after about two thirds of the length of the stave after which it declines slightly towards the end. This decline is most likely due to backflow of fresh cool air from the tube exit.

This discussion is deliberately brief, because most features of the distribution will also be present in the main setup, where they will be discussed. The major take

away from this pilot study is that this method of cooling produces results which are in a feasible range, meaning it sets the goal to further study the performance of this general method.

3.3 Calibration

Since the total sensor circuit produces about 1 W of power, we will look into what effect this has on the temperature distribution. To do this, no extra heating or air cooling will be added. The setup otherwise equals that of the previous pilot study. I tried to start the readout program immediately after turning the sensor circuit on. The room temperature was 22.0 °C.

Figure 24: Temperature distribution plot at 0 seconds, x-axis corresponds to the x position on the PCBs, one plotted line for each y-position on the PCBs

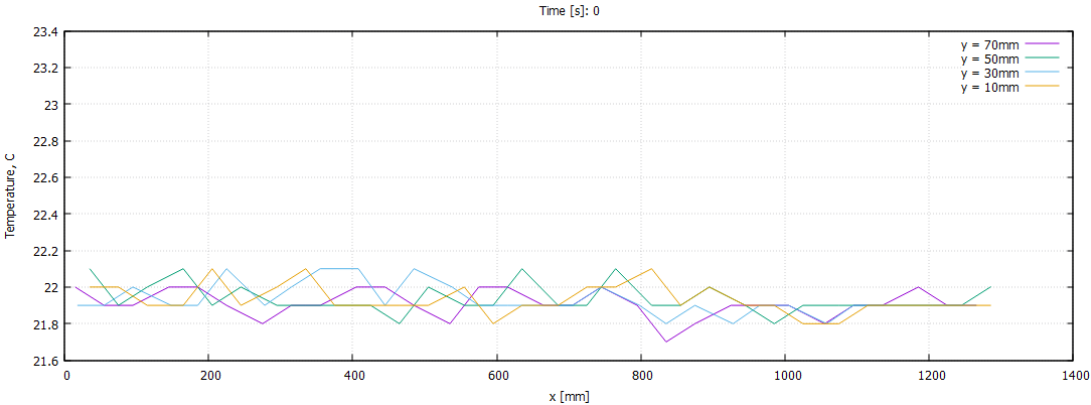The variation of the readings reflects the absolute calibration of the sensor, with peak-to-peak variation of about 0.3 °C.
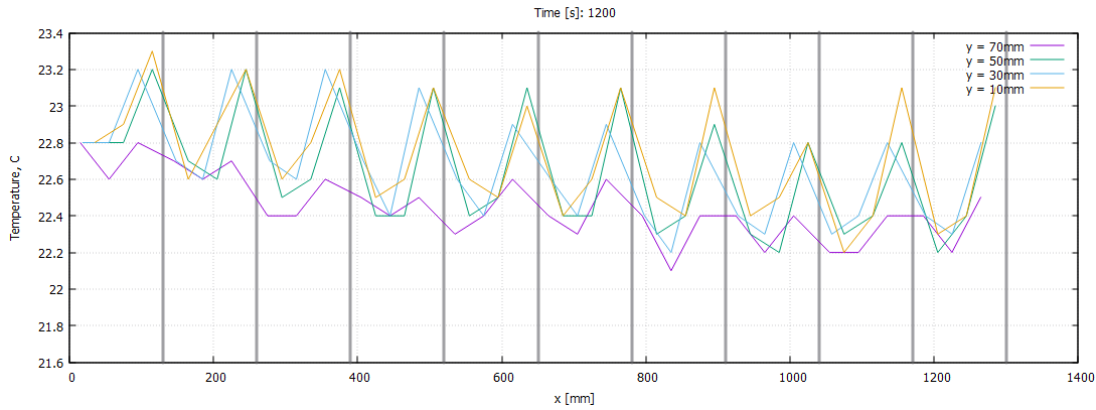
Figure 25: Temperature distribution plot after 20 minutes, x-axis corresponds to the x position on the PCBs, one plotted line for each y-position on the PCBs, vertical lines to mark PCB transitions

While the temperature distribution at 0 seconds equals the room temperature, the distribution after 20 minutes differs significantly. The overall temperature is slightly higher and we get one temperature spike for every PCB. In closer examination this spike sits exactly at the position of the FPGA on each PCB. This makes sense, since it contains the processing unit for the temperature readout.

To examine whether those temperature spikes are still noticeable in the experiments with the heating power turned on, we do the following: In the following experiments a jagged structure of the temperature distributions will be observed, which looks very similar to this. To see if this jagged structure is caused by the sensor circuit heat we compare the position of the minima/ maxima and find out that they are different.

To further solidify this, I wrote an addition to the data processing C++ file (see A), which averages over the temperatures at 0 seconds, then calculates the difference from the average for each sensor and then in the final step subtracts the sensor corresponding difference for all temperature entries. I then compared the plots of these new modified datasets to the original ones: the jagged structure did not vanish and the plots are basically unchanged in their structure, which means that something other then the sensor circuit heat is responsible for it. (The addition to the data processing C++ file will not be used outside of this calibration.)

We conclude that the sensor circuit power has no noticeable effect once the real

heating power is turned on, so it will not be taken into account for discussions any further.

3.4 Main setup

3.4.1 Setup

In this part new fans and their support structure, to fit inside the tube, are used.
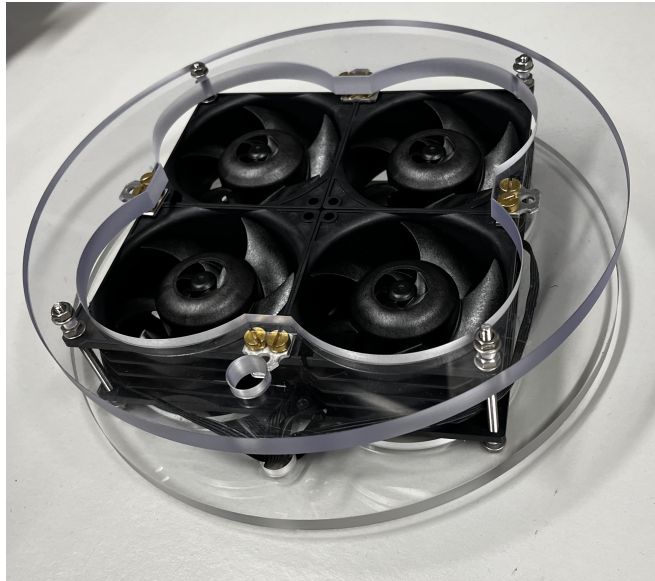
Figure 26: One of the two fan structures

Each module consists of four fans of the type [20]. They can individually be switched on and off and are run on 12 Volts DC with their speed being controlled via pulse-width modulation (PWM): a function generator is used to give out rectangular pulses with a constant frequency which are sent to the fans. The length of the pulses in percent of the period is controlled to set the power output - called the duty cycle.

This part contains three experimental setups. In the first one the fan structure is equipped to the right hand side of the tube with air being blown into the tube. In the second the left hand side is equipped with air being sucked out of the tube. In the third both sides are equipped with air again being moved from left to right. In all setups a single stave is mounted in the middle of the tube.

With the start of the experiment the fans were switched on as well as the heating power. The temperature readout ran for 600s. The duty cycle of all fans in all

three setups is 50%. The room temperature was 23.0 °C. The power output of the stave was 30.3 W. The air speed is measured using the anemometer at the 1m mark (middle of the tube) at different positions in the plane.
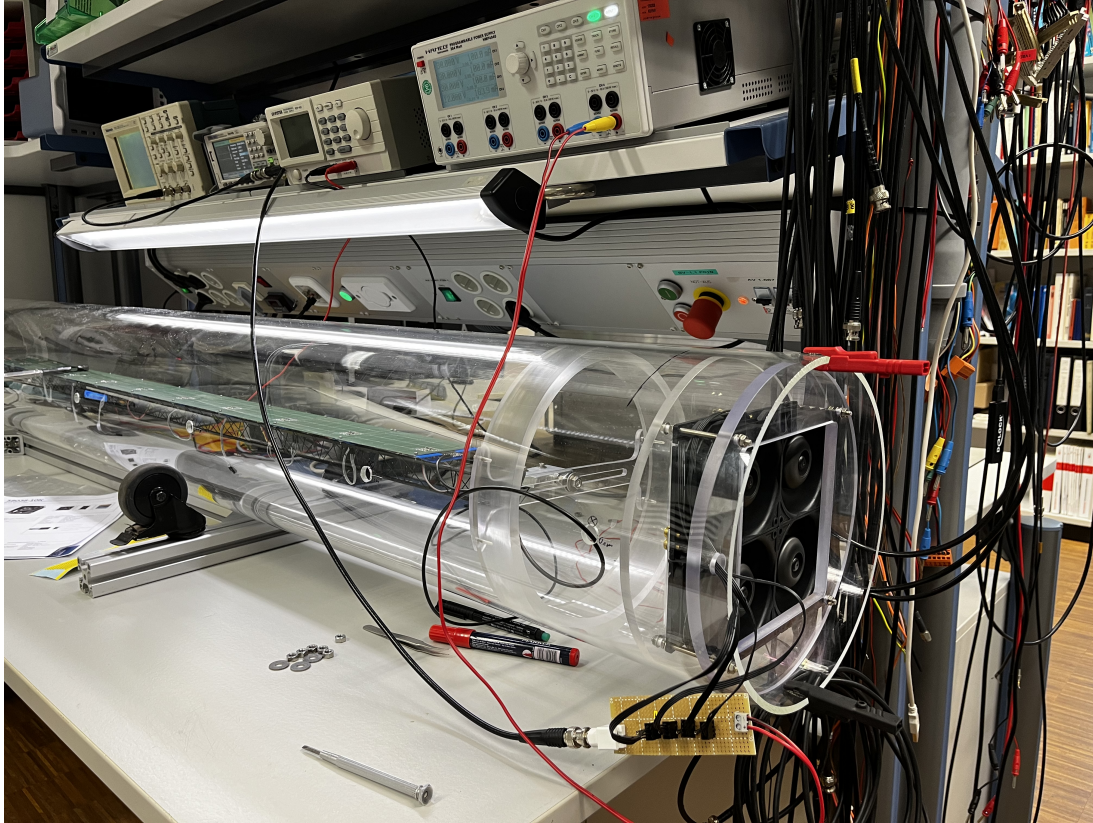
Figure 27: The complete setup with the right fan structure equipped

3.4.2   Results Setup 1

Due to the turbulent nature of the fluid flow the fluid speed varies greatly in time. As time averages are the relevant quantities, an average over the course of one minute is taken at each measured position. The air speed for the first setup (right hand side fan structure only) is measured to be roughly 2.3 m/s on average in the measured plane. The only major deviation from this is the speed inside the space frame, which is 1.6 m/s. Using equation 7 and the tube diameter as characteristic length, this makes for a Reynolds number of $Re \approx 36000$, which is well in the turbulent regime.

A static temperature distribution evolves:
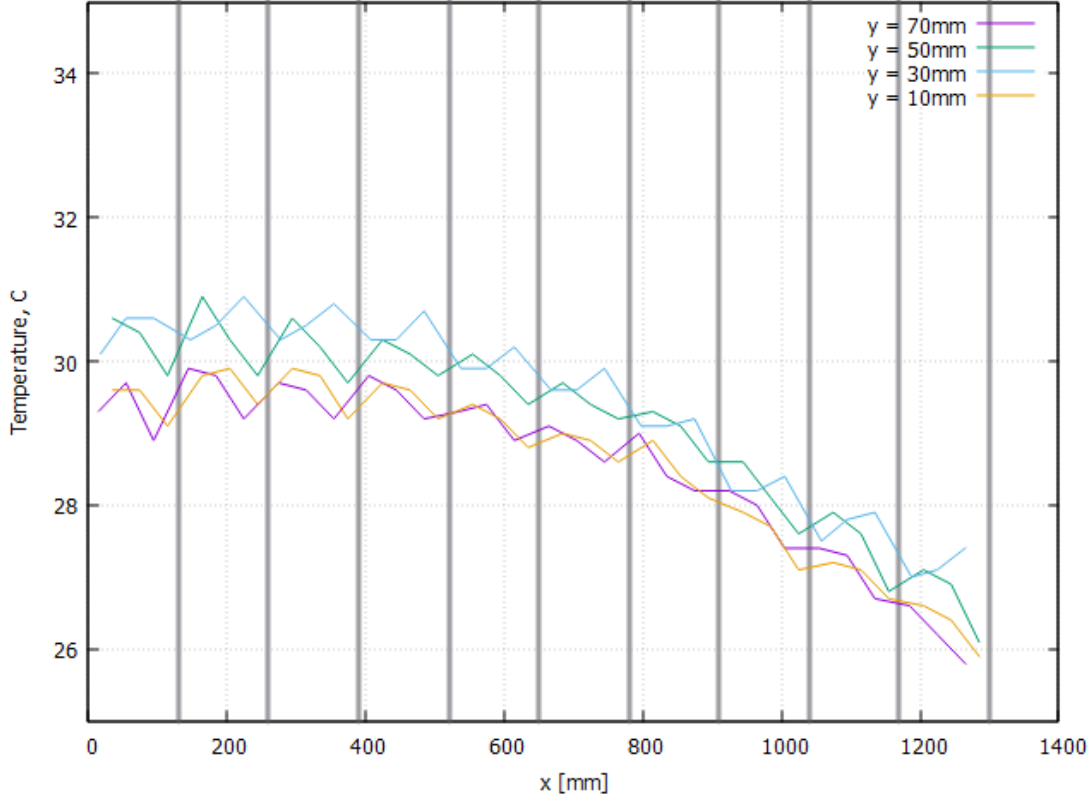
Figure 28: Right fan structure: temperature distribution plot of the PCB sensors at 10min (input temp.: 23.0 °C): x-axis corresponds to the x position on the PCBs, one plotted line for each y-position on the PCBs, vertical lines to mark PCB transitions

We can see a temperature rise from slightly above room temperature on the right side, where air is being blown into the tube. The maximum temperature of around 30°C is reached after about two thirds of the length of the stave after which it stagnates. To estimate the overall cooling performance we are interested in the maximum temperature reached at which the distribution stagnates, calling this the plateau temperature $T_{plateau}$, which we estimate by taking an average of the relevant region: $T_{plateau} = 30.5°C$. Since heat flux is linear to temperature difference, this will be our "performance indicator":

$$\Delta T = T_{plateau} - T_{ambient} = 7.5 \text{ K} \tag{21}$$

The temperature of the outer sides of the stave (represented by the 10 mm and 70 mm plot) is lower at all points, which makes sense due to the air speed on the

sides of the stave being higher than inside the space frame (middle of the stave). Also there is a "missing heat contributing part" on the edges, since the stave is not neighboured by additional staves in this experiment.

Every plotted line has a strongly jagged structure with an amplitude of order 0.5 to 1 °C. With the help of the vertical lines marking the PCB transitions, we can easily make out that there is exactly one maximum/ minimum per PCB. The minimum seems to be around the transition, with the exception of the 30 mm line, which is slightly shifted to the right. This can have a number of reasons. The first and most obvious one is that the edges of the PCBs do not contain any heating coils. This corresponds well with the position of the minima. The different minimum position of the 30 mm line can be explained by the presence of the hot spot created by the FPGA, which has that position on the PCB. This will be seen more clearly in section 3.5.

Another possible reason is that the space frame side of the stave is not flat, but has an irregular geometry with plastic bases sitting at the PCB transitions. Those can have two possible effects: heat can dissipate into the space frame at the base overlay. Also the flow profile can become irregular which leads to a different heat transfer coefficient. The effect of this is simulated in chapter 5.2.2.

3.4.3   Assessment of the temperature distribution

With the Reynolds number calculated, we know that this is best described as a fully turbulent internal convection problem. Since the PCBs are really thin, we will model them as a flat plate and can assume a uniform surface heat flux (heating power $+$ 1W from the sensor circuit) of:

$$q = \frac{P}{A} = \frac{30.3W + 1W}{2 * 0.08m * 10 * 0.13m} = 150.5 \text{ W/m}^2 \tag{22}$$

We will first calculate the bulk mean temperature increase of the cooling air. For a mean velocity of 2.3 m/s we can calculate the mass flow rate as:

$$\dot{m} = \rho v A = 1.2 kg/m^3 * 2.3m/s * \pi(0.12m)^2 = 0.125 \text{ kg/s} \tag{23}$$

Using equation 20, the room temperature of 23.0 °C, power output of 30.3 W and specific heat capacity of air $c_P = 1006 J k g^{-1} K^{-1}$, we get a temperature profile of:

$$T_b(x) = 23.0 \,°C + 0.25 \,°C/\text{m} * x \tag{24}$$

So the bulk mean temperature does not increase significantly throughout the tube, which means the temperature more or less stagnates after the flow is fully developed. Whether the flow is fully developed and if in what region, remains to be seen.

Using the turbulent estimates for entrance length 17 18, we get $X \approx 2.4$ m, which would mean that the flow is not fully developed at any point. This is however likely to be inaccurate, since the flow is created within the tube by the fan structures, as opposed to the theoretical fully uniform flow with uniform velocity coming from the outside of the tube. The fans create a velocity profile likely to be more similar to that of the fully developed flow, since the fan edges do not reach the outer diameter of the tube, thus not creating flow at the outer diameter.

The temperature profile of this experiment suggests that the fully developed region is reached after about two thirds of the stave, where the temperature then stagnates.

Now we will compare the surface-fluid temperature difference with the model for fully developed turbulent pipe flow. The Prandtl number of air using 8, dynamic viscosity of $\mu = 18.3 * 10^{-6}$ Pa s and a thermal conductivity of $k = 0.026 \text{W}/(\text{mK})$, is $Pr = 0.71$.

Using the previously calculated Reynolds number and 14 we get:

$$Nu = 0.023 * 36000^{0.8} * 0.71^{0.4} = 88 \tag{25}$$

Rearranging 9 and then back-solving Newtons law of cooling 2 for the temperature difference we finally get:

$$\Delta T = T_s - T_\infty = \frac{q}{h} = \frac{q \, L}{Nu \, k} = 15.8 \text{ K} \tag{26}$$

This is way off the experimental result of $\Delta T = 7.5K$. This is because we did not take into account the radiative heat transfer, which becomes significant for the

higher temperatures of the stave. The emissivity of the PCB and surroundings can be estimated as being equal. Using plateau temperature of 30.5 °C (from the experiment) and equation 3, we get:

$$q = \sigma * (T^4_{surface} - T^4_{ambient}) = \sigma * [(303.7\text{K})^4 - (296.2\text{K})^4] = 45.9\text{W/m}^2 \quad (27)$$

Now using the resulting $q' = (150.5 - 45.9)\text{W/m}^2 = 104.6\text{W/m}^2$, we get:

$$\Delta T = \frac{q' \, L}{Nu \, k} = 11.0 \text{ K} \quad (28)$$

This is a better estimate, considering the experiment is far from the theoretically "perfect geometry". The biggest uncertainty here lies in the estimated Reynolds number, which we seem to have slightly underestimated. The estimate we used, is that for a smooth pipe - our tube on the other hand features the stave in the middle forming obstacles for the flow, which cause increased turbulence.

3.4.4 Results of Setup 2 and 3

The air speed for the second setup (left side fan structure only) is measured to be slightly lower with roughly 2.1 m/s on average in the measured plane, the speed inside the space frame being 1.5 m/s.

Figure 29: Left fan structure: temperature distribution plot of the onboard sensors on the PCBs after 10 minutes (input temp.: 23.0 °C), x-axis corresponds to the x position on the PCBs, one plotted line for each y-position on the PCBs, vertical lines to mark PCB transitions

We calculate the plateau temperature of $T_{plateau} = 31.0°C$ and get:

$$\Delta T = T_{plateau} - T_{ambient} = 8.0K \tag{29}$$

The air speed for the third setup (both fan structures) is measured to be slightly higher with roughly 2.4 m/s on average in the measured plane, the speed inside the space frame being 1.8 m/s.
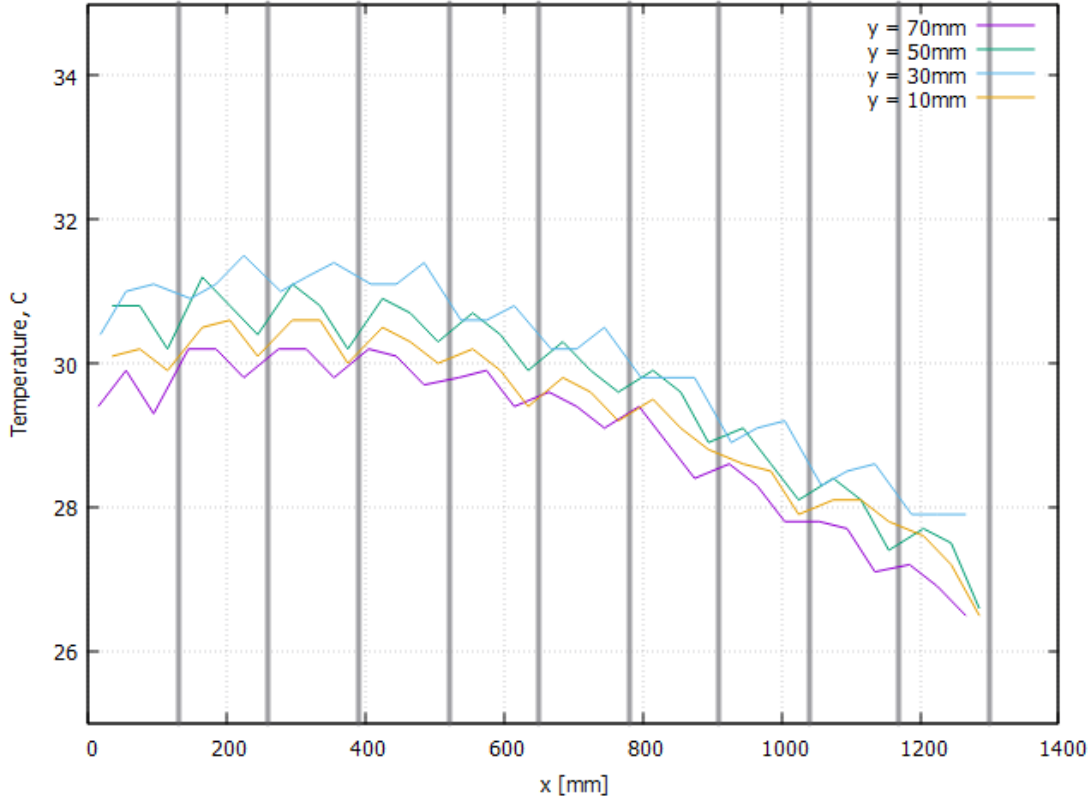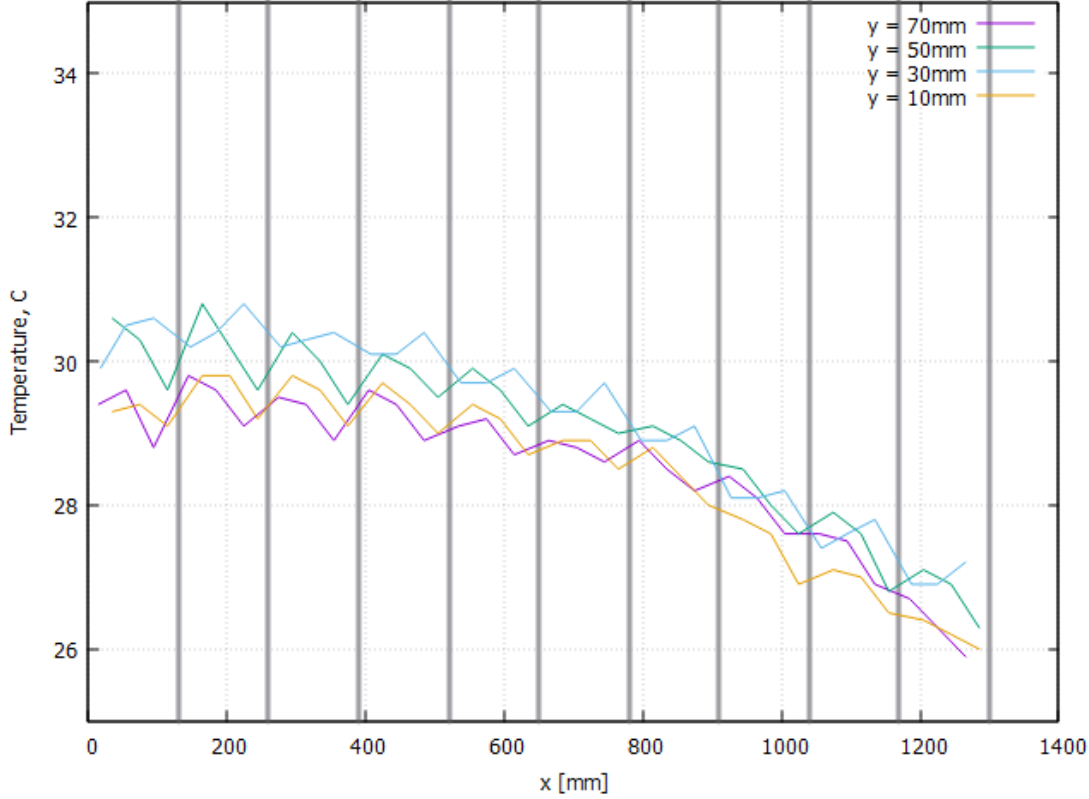
Figure 30: Both fan structures: temperature distribution plot of the onboard sensors on the PCBs after 10 minutes (input temp.: 23.0 °C), x-axis corresponds to the x position on the PCBs, one plotted line for each y-position on the PCBs, vertical lines to mark PCB transitions

We calculate the plateau temperature of $T_{plateau} = 30.3°C$ and get:

$$\Delta T = T_{plateau} - T_{ambient} = 7.3K \tag{30}$$

Summarizing, all fan setups perform almost the same. The second setup with the air being sucked into the tube performs the worst, while the double fan structure setup only outperforms the first setup by a small amount, despite using double the fan power.

To explain this "underperformance", we have to take a look at the fans specification sheet [20]: their maximum volumetric flow is given as 173.3 m³/h. With a duty cycle of 50 percent, we get roughly 5500 rpm, which is 55 percent of the maximum of 10000 rpm, resulting in an estimated maximum volumetric flow of 95.3 m³/h per fan. Now calculating the average velocity of four fans for the give cross section, amounts to: $v_{average} = 2.34m/s$ which is close to our measured average velocity.

This means that the flow can be estimated as having no significant pressure drop. While adding fans in series, like it is done in this third setup, increases the maximum air pressure drop possible, it does not increase the maximum possible volumetric flow, which is already reached with the four fans from setup 1.

3.5 Thermal imaging camera

To get a sense of any potential blind spots on the PCBs (areas not well covered by the onboard sensors) and an understanding on how well heat dissipates into the space frame structure, a thermal imaging camera is used. Since some wavelengths of infrared radiation do not pass through acrylic glass, to conduct the experiment a stave is placed outside the tube and heated with 30.4 W until a static temperature distribution is reached. There are no forced air cooling measures used.

It is important to note that in this section only the qualitative temperature distribution is of interest and no discussion of quantitative values will be made.
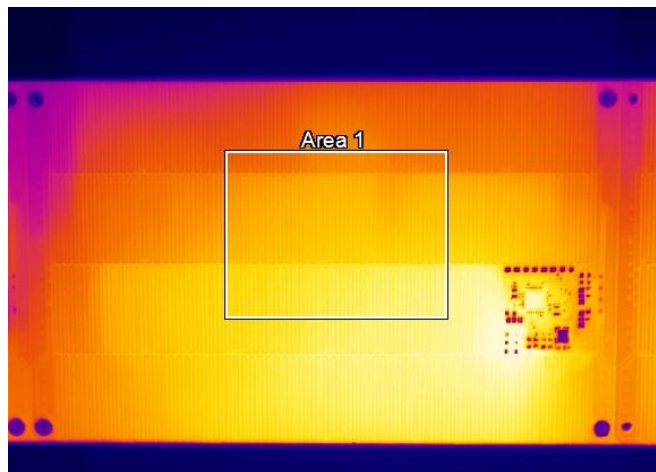
Figure 31: Top heat camera view of a PCB

There are two striking features: the hot spot at the position of the FPGA and the colder sections at the transition edge between PCBs. The (top and bottom) sides of the PCB are also slightly colder, this is, however, expected since there are no adjacent heat contributing boards.

As explained in section 3.1, to make up for the missing heating coils in the section of the FPGA, resistors are placed at the position. The exact position is, however, not the middle of the FPGA but the bottom left, which one can easily make out

as the center of the hot spot, which results in the observed hot spot.

The colder sections at the transition edge arises from the fact that 5mm on each side of the PCB contain no heating coils. This shows that the missing heating coils are a major contributing factor to the jagged structure of the temperature distribution plots (as apposed to other reasons such as variation of air flow along the stave).
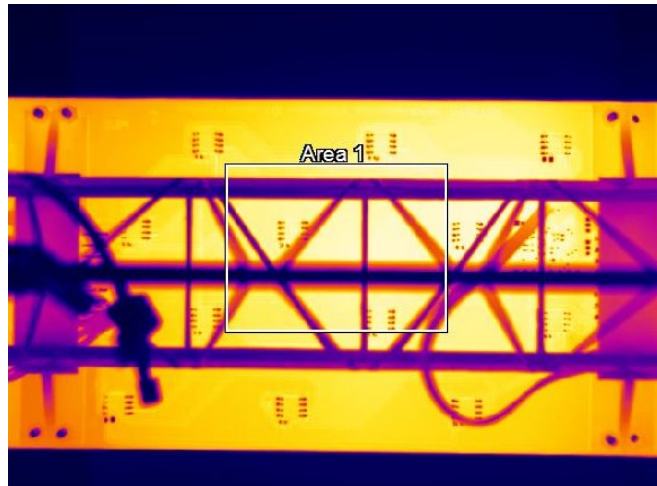
Figure 32: Heat camera view of the space frame and the bottom side of the PCB

While the plastic bases (on which the PCBs are screwed) reach a significant temperature, the spaceframe remains almost at room temperature. This means that the cooling factor coming from heat dissipation into the spaceframe and bases (which would then have a larger surface area to dissipate heat into the surrounding air) is very small.

3.6 Two staves

3.6.1 Setup

A second stave is used in this experiment. The new stave is identical to the one described in section 3.1, except that it has no equipped temperature sensors and is therefore only used for heating. The idea behind this experiment is to test the influence of neighbouring heat producing staves on the temperature of the main stave, since this will also be the case in the detector.

The new heating stave is placed on the edge of the tube with the main stave next

to it in the middle of the tube (since the inner diameter of the tube is 24 cm and the width of a stave is 8 cm, there are a theoretical three slots for the staves inside the tube. Since there were not any grave differences between setups in section 3.4, we settle for the easiest option and equip only the right fan structure (air being blown into the tube).

With the start of the experiment the fans are switched on as well as the heating power. The temperature readout went on for 1200s. The duty cycle of all fans in all setups is 50%. The room temperature was 23.5 °C. The power output of the staves was 30.1 W each. The air speed is measured using the anemometer at the 1m mark (middle of the tube) at different positions in the plane.
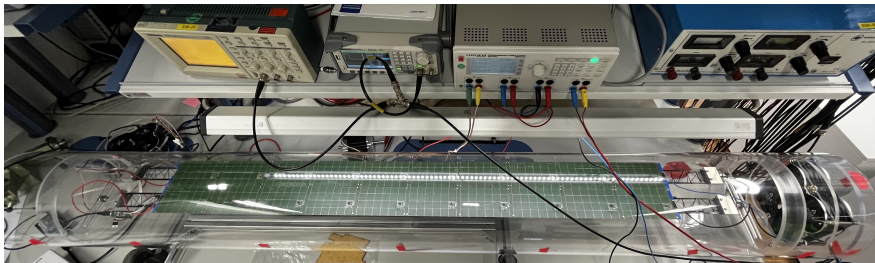
Figure 33: The complete setup

3.6.2   Results

The air speed for this setup is measured again to be roughly 2.3 m/s on average in the measured plane. The only major deviation from this is the speed inside the space frame, which is 1.6 m/s, which is the same as in the main setup, which we expected. The only difference is that we measure small difference in velocity laterally: the velocity on the right hand side (over the additional heating stave, side of the 70mm line) being slightly higher ($\approx$ 0.2 m/s) with respect to the left side (no stave).
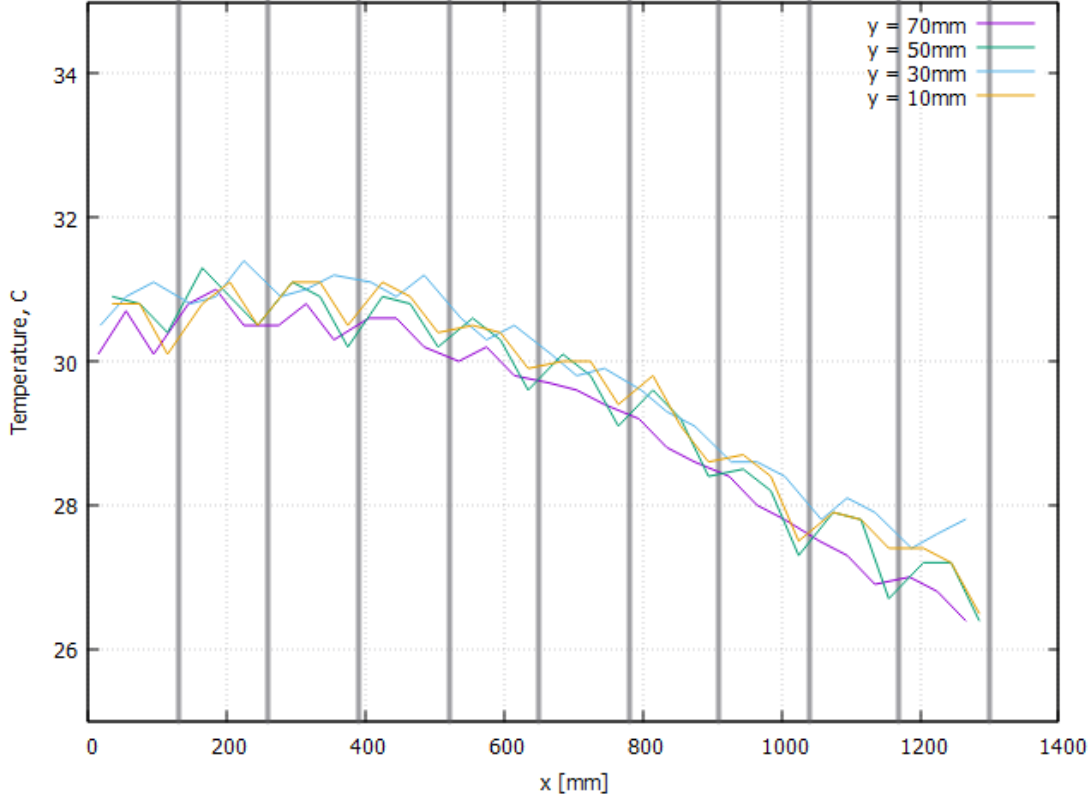
Figure 34: temperature distribution plot of the onboard sensors on the PCBs after 20 minutes (input temp.: 23.5 °C), x-axis corresponds to the x position on the PCBs, one plotted line for each y-position on the PCBs, vertical lines to mark PCB transitions

We expected the 70mm temperature line (adjacent to the second stave) to now be on the same level as the middle PCB 30mm and 50mm lines, which is the case. The air temperature distribution in close vicinity to the PCBs (in the plane perpendicular to the stave axis) can now be assumed to be more uniform. Surprisingly, the 10mm line on the opposite side is now also on par with the middle lines. This is probably due to the measured slightly lower fluid speed on this side, resulting in slightly worse cooling.

We calculate a plateau temperature of $T_{plateau} = 30.9°C$ and get:

$$\Delta T = T_{plateau} - T_{ambient} = 7.4K \tag{31}$$

This is only a minor deviation from the previous experiment with one stave. Concluding this experiment we can say that the addition of staves does not

significantly alter the overall cooling performance, meaning a single stave is a good estimate for the a full barrel of adjacent staves.

3.7 Split tube

3.7.1 Setup

For this experiment we are set to split the tube lengthwise in a top and bottom half alongside the staves edges. The idea behind this is to find any difference in cooling performance of the top versus bottom side. Also this provides the base of the next experiment, where a new cooling idea is tried.

To achieve this I designed multiple stencils, which were then laser cut from thin (3mm) laminar wood. The cutouts were then screwed onto the spaceframe and PCBs of the heating and main stave. The main stave is again in the middle. The complete structure was designed to fit exactly into the tube with no gaps.

Figure 35: The wood cutouts screwed to the stave
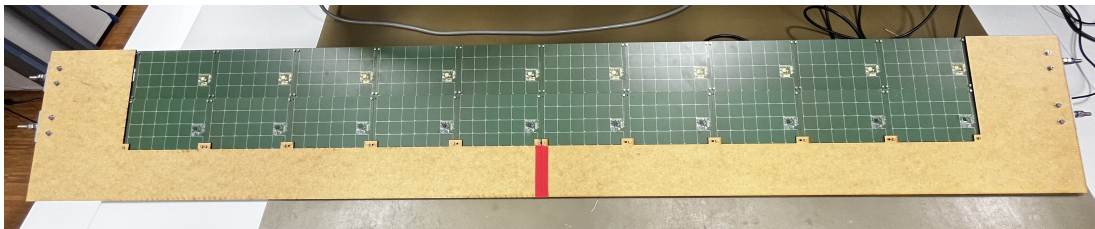
The mounting brackets (figure 18) were no longer needed in this experiment, since the structure supports itself on the tube walls. Extra cutouts were then used to be fitted into space between the end of the staves and the fan structures. In this experimented I chose to use both fan structures, since they will also be needed for chapter 3.8.
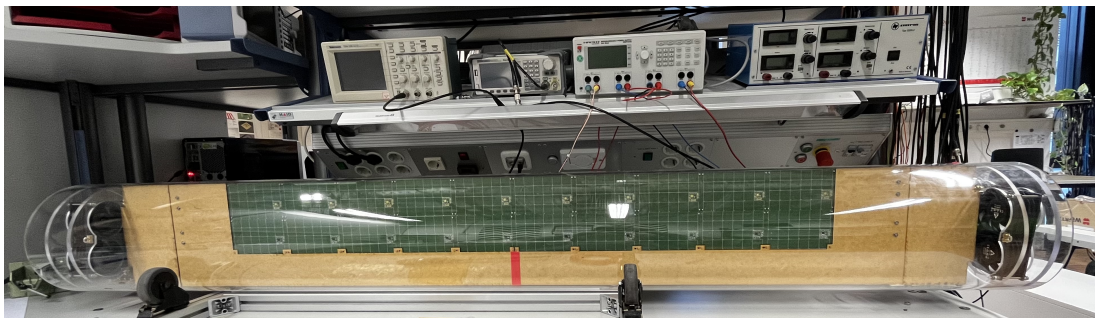

Figure 36: The complete setup

This part contains three experimental setups. In the first one all fans are operated. This is the same as in the main setup in chapter 3.4, to give insights on how the wood cutouts impact the air flow and general performance. In the second part only the bottom two fans on each side are operated so there only is an airflow in the bottom half. In the third part then only the top two fans on each side are operated so there only is an airflow in the top half.

With the start of the experiment the fans were switched on as well as the heating power. The temperature readout ran for 600s. The duty cycle of all fans in all setups is 50%. The room temperature was 22.6 °C. The power output of the stave was 30.1 W per stave. The air speed is measured using the anemometer at the 1m mark (middle of the tube) at different positions in the plane.

3.7.2 Results

The air speed for this setup is measured again to be about 2.3 m/s on average in the measured plane. The speed inside the space frames being roughly 1.8 m/s. We measure a bigger difference in velocity laterally: this time the velocity is higher on the side of the wooden separator ($\approx$ 0.4 m/s), which is the one on the 10mm line side. I do not have an explanation for this lateral difference anomaly other than saying that it is induced by the not completely uniform geometry of the setup.

In all three setups the line temperature rises from this side (10mm line) to the other (70mm line). This is in accordance with the measured velocity difference and air temperature difference due to the extra stave.

Figure 37: Setup 1: flow in both halves: temperature distribution plot after 10 minutes (input temp.: 22.6 °C), x-axis corresponds to the x position on the PCBs, one plotted line for each y-position on the PCBs, vertical lines to mark PCB transitions

The temperature distribution has a prominent "bump" on the right hand side. This is most likely due to the cutout separator piece which is fit directly to the fan structure. It had to be slightly angled to properly fit. This would also explain why the "bump" is more prominent on the bottom half distribution as in respect to the top half distribution in which the cutout is angled the other way.

We calculate the plateau temperature $T_{plateau,1} = 30.5°C$ and get:

$$\Delta T_1 = T_{plateau} - T_{ambient} = 7.9K \tag{32}$$

Regarding the plateau region of the temperature distributions this setup performs slightly worse than previous experiments. This is probably because of the more irregular flow in this experiment.

Figure 38: Setup 2: flow in the bottom halve: temperature distribution plot after 10 minutes (input temp.: 22.6 °C), x-axis corresponds to the x position on the PCBs, one plotted line for each y-position on the PCBs, vertical lines to mark PCB transitions
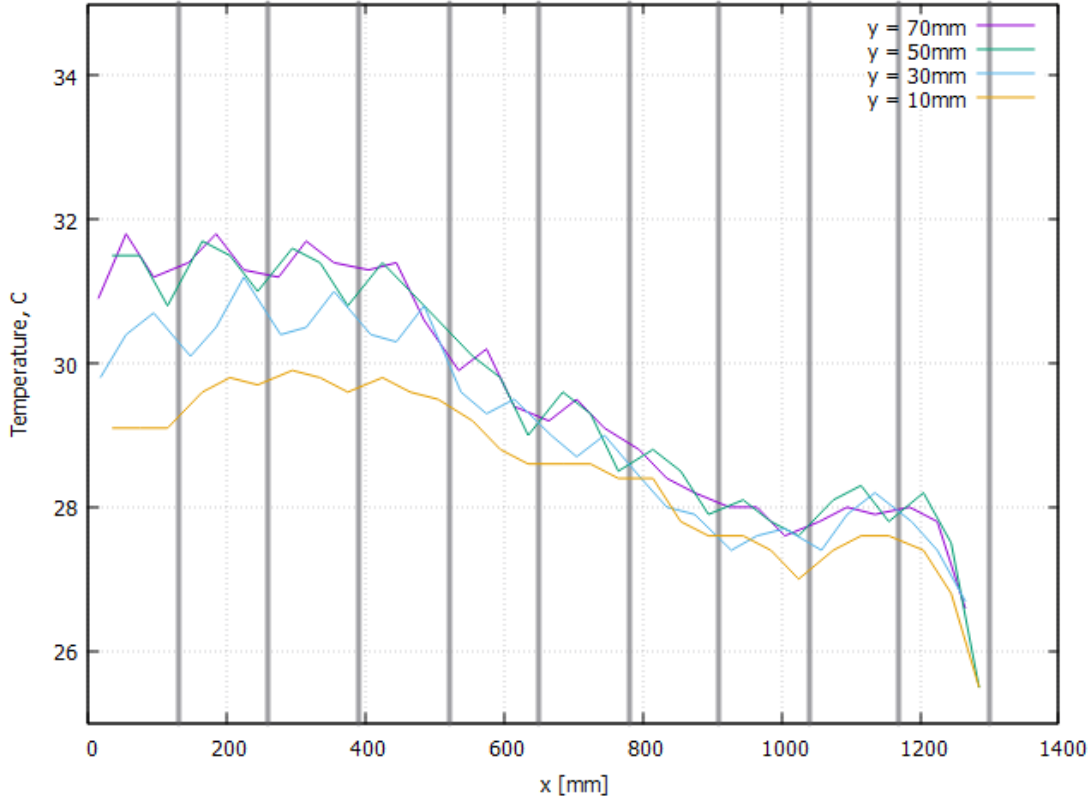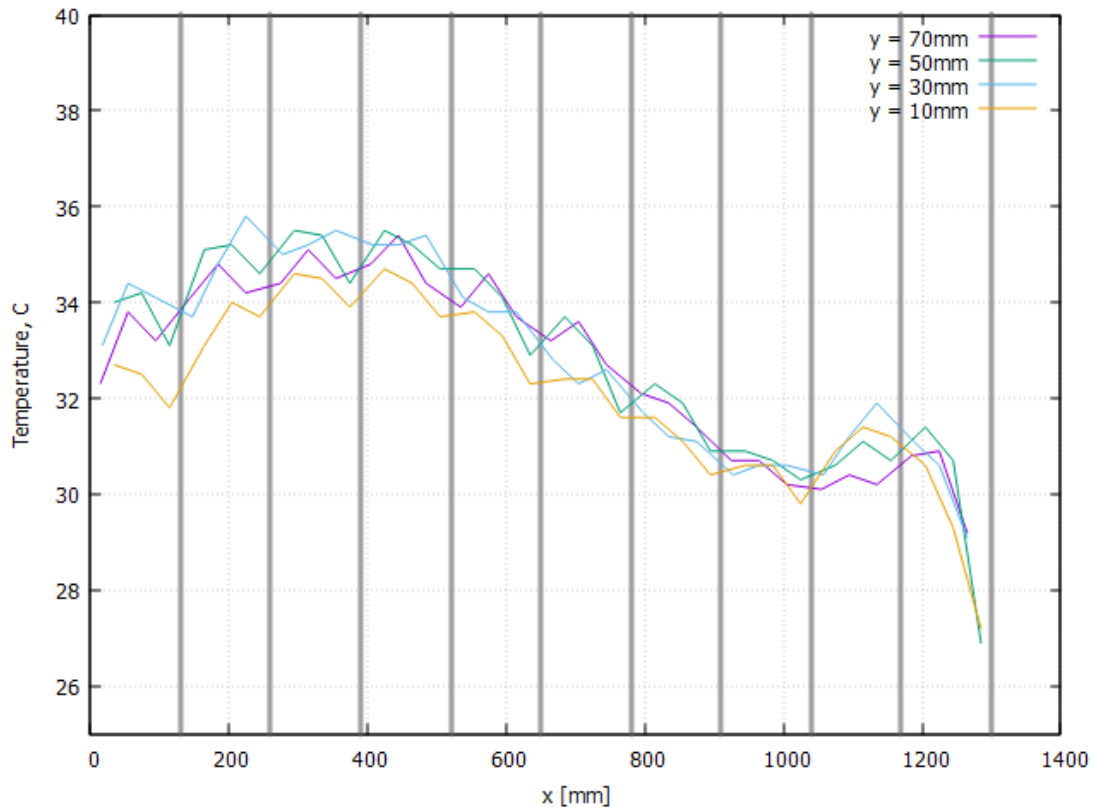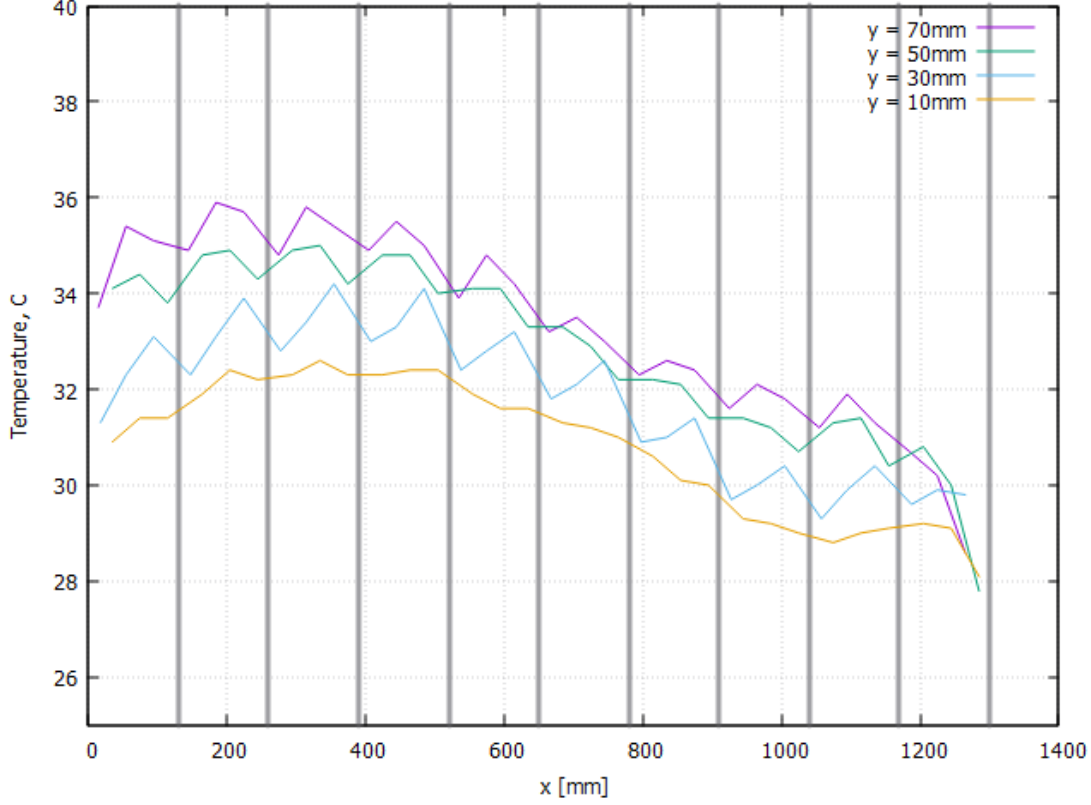
Figure 39: Setup 3: flow in the top halve : temperature distribution plot after 10 minutes (input temp.: 22.6 °C), x-axis corresponds to the x position on the PCBs, one plotted line for each y-position on the PCBs, vertical lines to mark PCB transitions

The temperature distribution of setup 2 and 3 both fall off towards the end. This is most likely due to backflow through the switched-off fans on the respective other side of the split tube. We calculate a plateau temperature of $T_{plateau,2} = 34.8°C$ and get:

$$\Delta T_2 = T_{plateau} - T_{ambient} = 12.2K \tag{33}$$

and for the third setup a plateau temperature of $T_{plateau,3} = 34.3°C$ and get:

$$\Delta T_3 = T_{plateau} - T_{ambient} = 11.7K \tag{34}$$

Both halves perform almost the same, with setup 3 performing only slightly better than setup 2. This is however unexpected because the velocity close to the PCBs on the bottom half (measured velocity inside the space frame) is significantly lower than the velocity over the top halve. This should result in significantly lower

cooling performance of the bottom halve. The reason this is not the case has to be increased turbulence on the bottom halve due to the space frame acting as an obstacle. This will also be shown in a simulation in 5.2.2.

Another piece of information to take away from setup 3 is that the jagged structure of the distribution is still there and nearly unaltered. If the jagged structure was solely a result of irregularities in fluid flow (caused by the stave frame), we would have expected it to vanish completely and give a smooth distribution, since on the top halve there can be no irregularities in the flow. This is however not the case which proofs that the missing heating coils are the major contributor to the jagged structure. The only noticeable difference is that the minimum position of this setup is very slightly shifted to the right, which then on the opposite will be the result of the (in this setup not existing) variation of fluid flow.

3.8 Split flow and counterflow

3.8.1 Setup

The idea of this experiment is to achieve a lower temperature gradient by reversing the flow in the bottom half in respect to the upper half. To achieve this the fan structure is rebuild: two of the four fans are simply turned around (The fan structure was designed with the idea of being able to do this!). The rest of the setup remains the same as in section 3.7.

With the start of the experiment the fans were switched on as well as the heating power. The temperature readout ran for 600s. The duty cycle of all fans is 50%. The room temperature was 23.4 °C. The power output of the stave was 30.1 W per stave. The air speed is measured using the anemometer at the 1m mark (middle of the tube) at different positions in the plane.

3.8.2 Results

The air speed for this setup is measured to be roughly 2.4 m/s on average in the measured plane in both halves. The speed inside the space frames being roughly 1.8 m/s. As in the previous experiment we measure a lateral difference in velocity. The fact that the velocity stayed the same in this experiment proofs that our separating structure is pretty leak tight - if there would have been major leaks

in the tube separation directing the flow in opposite directions would not have worked that well.
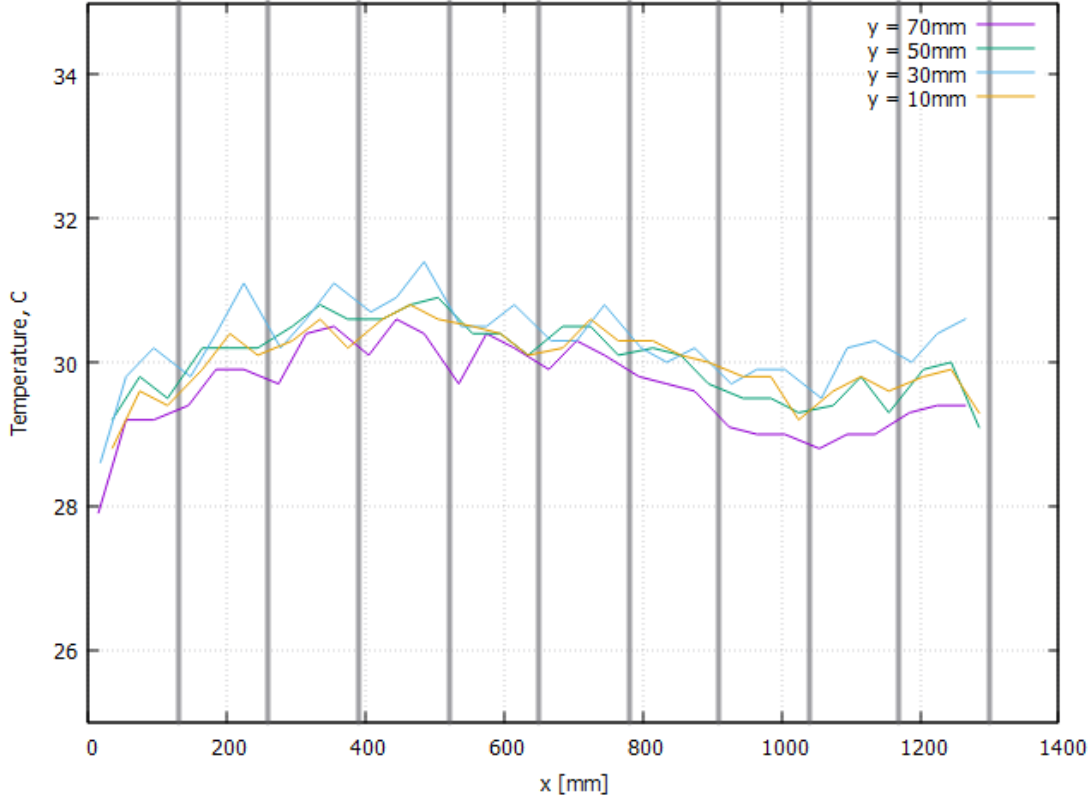
Figure 40: temperature distribution plot after 10 minutes, x-axis corresponds to the x position on the PCBs (input temp.: 23.4 °C), one plotted line for each y-position on the PCBs, vertical lines to mark PCB transitions

The setup performs as planned: While we sacrifice the cold temperatures at the entry region, a temperature distribution forms with a maximum peak to peak difference of only $\approx 3K$, which is much lower than in previous experiments. We calculate a plateau temperature of $T_{plateau} = 30.6°C$ and get:

$$\Delta T_2 = T_{plateau} - T_{ambient} = 7.2K \tag{35}$$

This is the best cooling performance so far, although only by a small margin.

3.9 Variation in air speed

3.9.1 Setup

In this experiment we analyze the variation of cooling performance versus a change in fluid speed. To do this three setups are tested with fan duty cycles of 20%, 50% and 100%. The setup is otherwise the same as in section 3.6.

A quick note to the fan structures: before this experiment the fan structures were slightly improved by widening the cutouts in the structure. Figure 3.4.1 actually shows this new improved structure. The previous cutout was rectangular and slightly protruded over the fan edges. Due to this improved airflow, the experiment in 3.6 is repeated to give a new point of reference. The new fan structures are also used in the next experiment (section 3.10).

With the start of each experiment the fans were switched on as well as the heating power. The temperature readout ran for 600s. The room temperature was 23.7 °C. The power output of the stave was 30.1 W per stave in the 50% setup, 30.6 in the 20% setup and 29.9 in the 100% setup. The air speed is measured using the anemometer at the 1m mark (middle of the tube) at different positions in the plane.

3.9.2 Duty cycle vs fluid speed

To quantitatively determine the real fan performance in respect to the duty cycle, I made a series of velocity measurements with the setup. The position for these measurements was fixed 2cm above the middle stave. In addition to the time average, I noted minimum and maximum measured velocity.

Figure 41: Duty cycle vs fluid speed
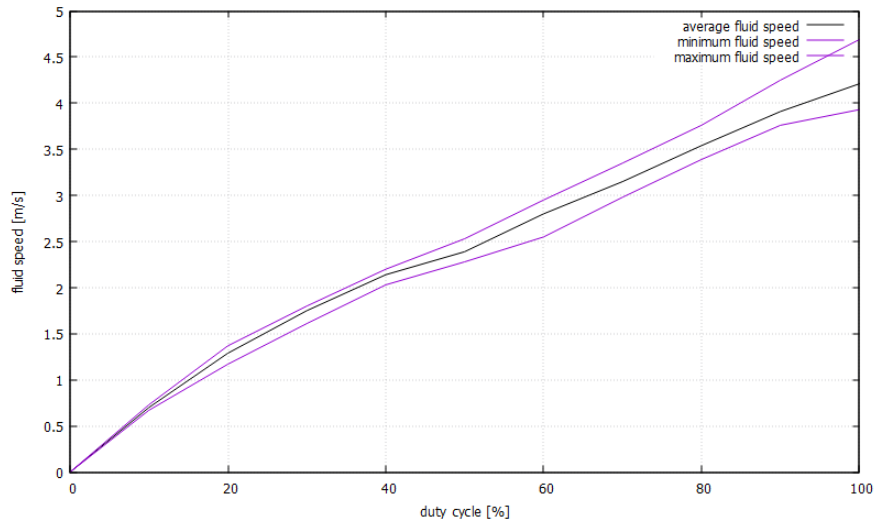
The relation is close to linear above $\approx 20\%$ duty cycle. It is also interesting to see that the deviation of minimum and maximum velocity from the average rises with increased fluid speed. This is an easily notable effect of rising turbulence!

3.9.3 Results: 20% duty cycle

We measure an average fluid velocity of 1.3 m/s. Using 7, we calculate a Reynolds number of Re = 20000.

Figure 42: 20% duty cycle: temperature distribution plot after 10 minutes (input temp.: 23.7 °C), x-axis corresponds to the x position on the PCBs, one plotted line for each y-position on the PCBs, vertical lines to mark PCB transitions

We get a plateau temperature of $T_{plateau,20} = 35.6°C$, and therefore:

$$\Delta T_{20} = 11.9K \tag{36}$$

Using 3 we now calculate the radiative heat flux at the plateau and the residual heat flux:

$$q = \sigma * (T^4_{surface} - T^4_{ambient}) = 75.0W/m^2 \tag{37}$$

$$q' = \frac{P}{A} - q_{radiative} = (151.9 - 75.0)W/m^2 = 76.9W/m^2 \tag{38}$$

We continue by using 14 to calculate the Nusselt number:

$$Nu_{20} = 55 \tag{39}$$

45

and calculate the temperature difference like previously shown in 26:

$$\Delta T_{theoretical,20} = \frac{q\,L}{Nu\,k} = 12.9K \tag{40}$$

This is slightly above the experimental value by 1 K.

3.9.4 Results: 50% duty cycle

We measure an average fluid velocity of 2.5 m/s. Using 7, we calculate a Reynolds number of Re = 39000.
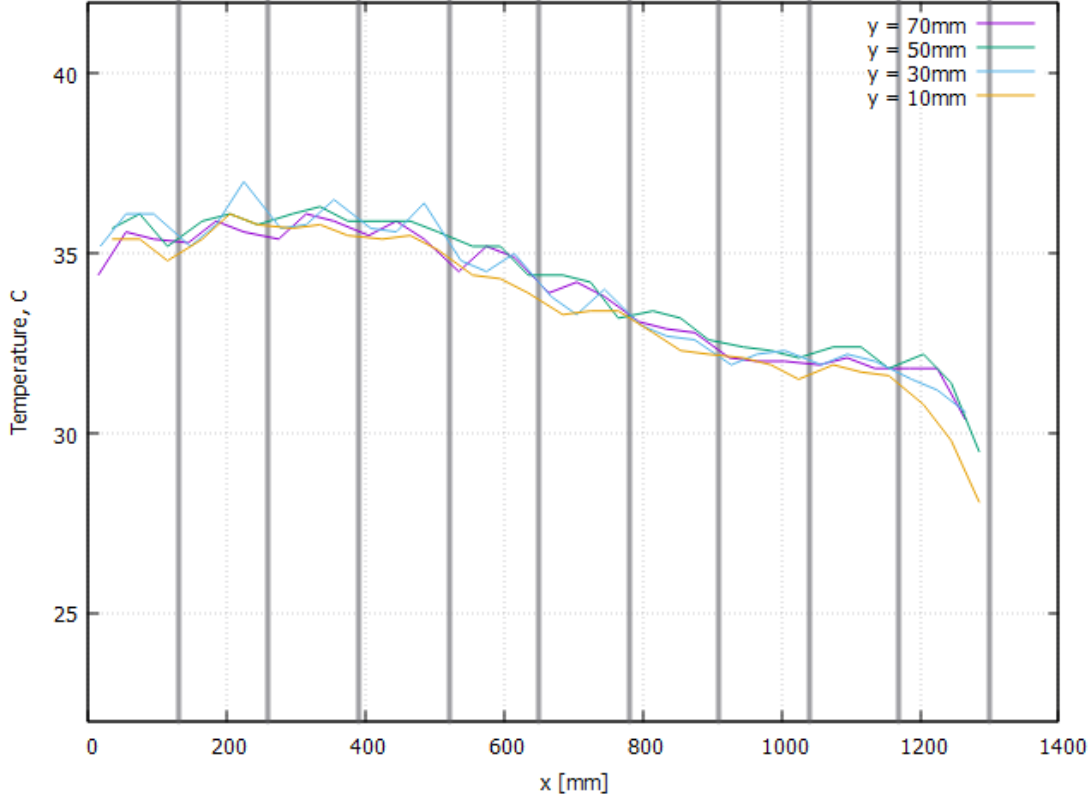

Figure 43: 50% duty cycle: temperature distribution plot after 10 minutes (input temp.: 23.7 °C), x-axis corresponds to the x position on the PCBs, one plotted line for each y-position on the PCBs, vertical lines to mark PCB transitions

We get a plateau temperature of $T_{plateau,50} = 30.8°C$, and therefore:

$$\Delta T_{50} = 7.1K \tag{41}$$

Using 3 we now calculate the radiative heat flux at the plateau and the residual heat flux:

$$q = \sigma * (T_{surface}^4 - T_{ambient}^4) = 43.7 W/m^2 \tag{42}$$

$$q' = \frac{P}{A} - q_{radiative} = (149.5 - 43.7)W/m^2 = 105.8 W/m^2 \tag{43}$$

We continue by using 14 to calculate the Nusselt number:

$$Nu_{50} = 95 \tag{44}$$

and calculate the temperature difference like previously shown in 26:

$$\Delta T_{theoretical,50} = \frac{q\,L}{Nu\,k} = 10.3K \tag{45}$$

This is again slightly above the experimental value.

3.9.5   Results: 100% duty cycle

We measure an average fluid velocity of 4.5 m/s. Using 7, we calculate a Reynolds number of Re = 71000.
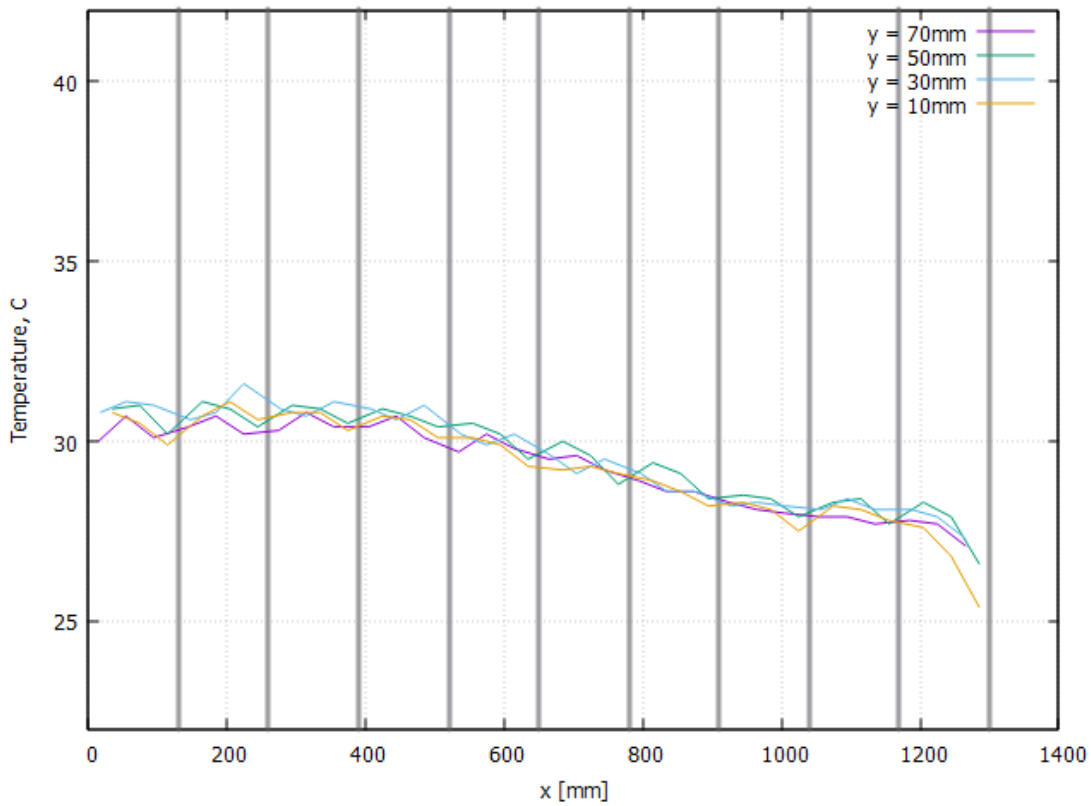
Figure 44: 100% duty cycle: temperature distribution plot after 10 minutes (input temp.: 23.7 °C), x-axis corresponds to the x position on the PCBs, one plotted line for each y-position on the PCBs, vertical lines to mark PCB transitions

We get a plateau temperature of $T_{plateau,100} = 28.5°C$, and therefore:

$$\Delta T_{100} = 4.8K \tag{46}$$

Using 3 we now calculate the radiative heat flux at the plateau and the residual heat flux:

$$q = \sigma * (T_{surface}^4 - T_{ambient}^4) = 27.9 W/m^2 \tag{47}$$

$$q' = \frac{P}{A} - q_{radiative} = (148.6 - 27.9)W/m^2 = 120.7 W/m^2 \tag{48}$$

We continue by using 14 to calculate the Nusselt number:

$$Nu_{100} = 152 \tag{49}$$

and calculate the temperature difference like previously shown in 26:

$$\Delta T_{theoretical,100} = \frac{q\,L}{Nu\,k} = 7.3K \tag{50}$$

This is again slightly above the experimental value, showing that while the calculated estimates are not exact, they scale consistently with varying air speed.

3.10   Variation of heating power

3.10.1   Setup

To get a sense of how the temperature distribution scales with heating power, this experiment with doubled power output is executed. The setup is otherwise the same as in section 3.6.

With the start of the experiment the fans were switched on as well as the heating power. The temperature readout ran for 600s. The duty cycle of all fans is 50%. The room temperature was 23.7 °C. The power output of the stave was 60.3 W per stave. The air speed is measured using the anemometer at the 1m mark (middle of the tube) at different positions in the plane.

3.10.2   Results

We measure an average fluid velocity of 2.5 m/s. Using 7, we calculate a Reynolds number of Re = 39000.

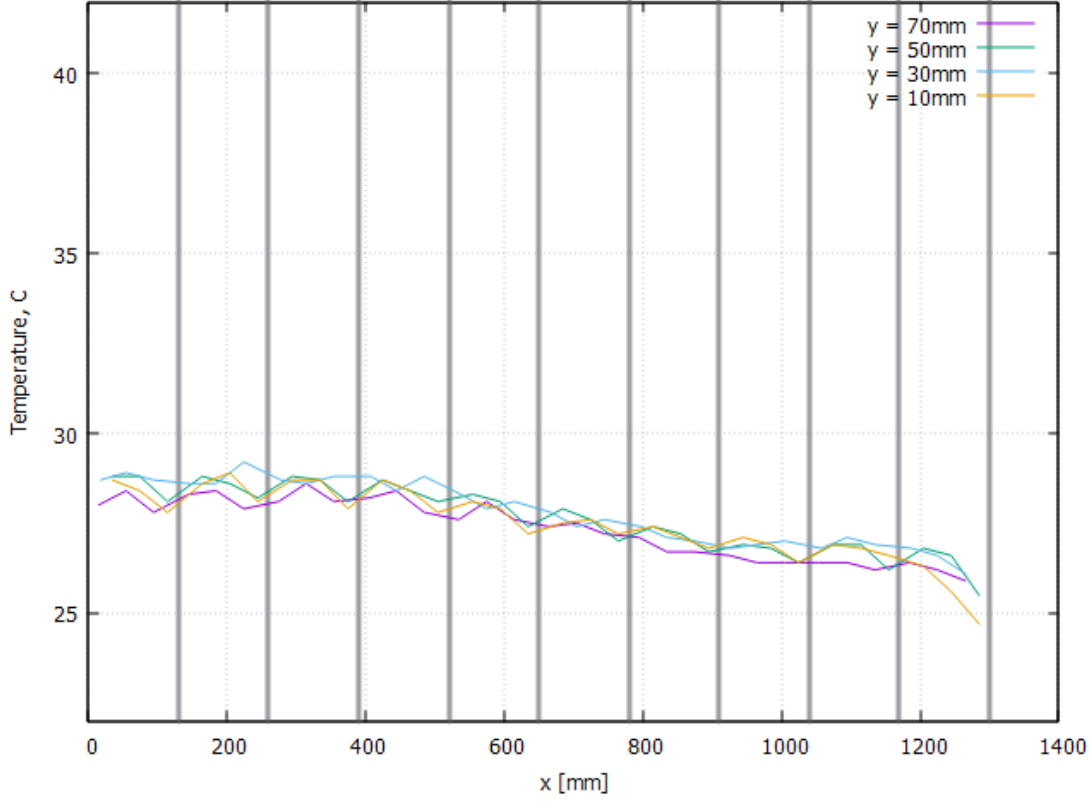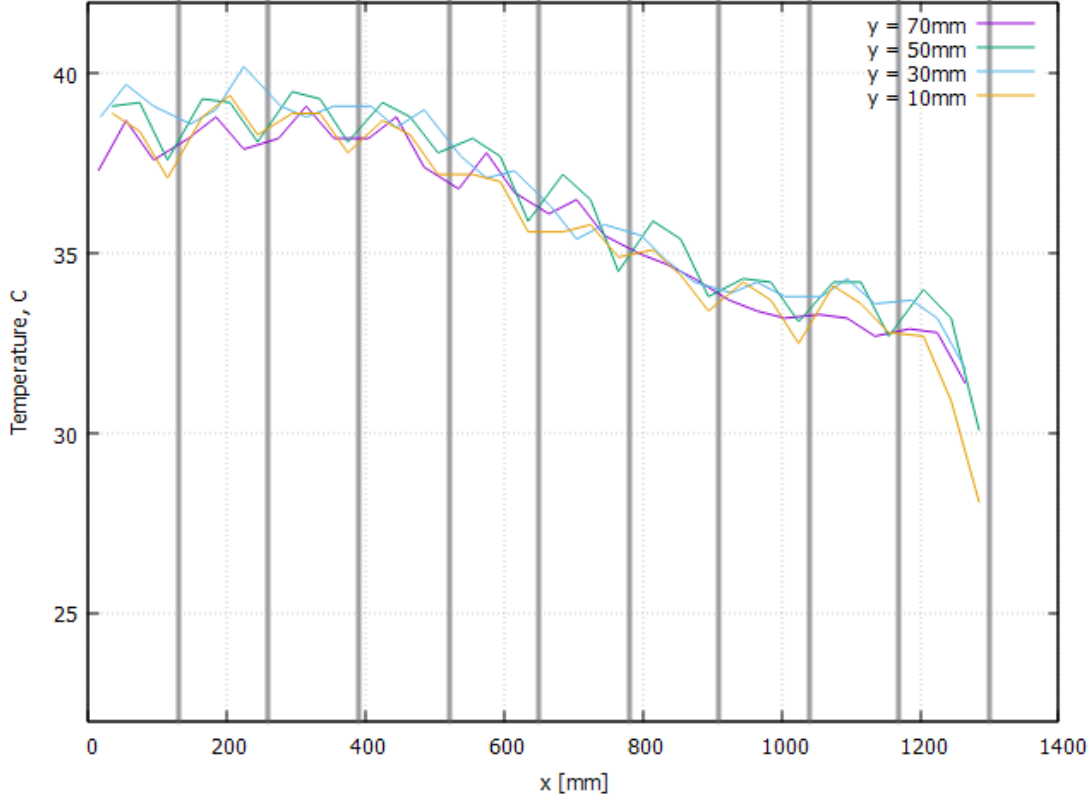Figure 45: Doubled heating power: temperature distribution plot after 10 minutes (input temp.: 23.7 °C), x-axis corresponds to the x position on the PCBs, one plotted line for each y-position on the PCBs, vertical lines to mark PCB transitions

We get a plateau temperature of $T_{plateau,P} = 38.8°C$, and therefore:

$$\Delta T_P = 15.1K \tag{51}$$

Using 3 we now calculate the radiative heat flux at the plateau and the residual heat flux:

$$q = \sigma * (T^4_{surface} - T^4_{ambient}) = 96.7W/m^2 \tag{52}$$

$$q' = \frac{P}{A} - q_{radiative} = (289.9 - 96.7)W/m^2 = 193.2W/m^2 \tag{53}$$

We continue by using 14 to calculate the Nusselt number:

$$Nu_P = 95 \tag{54}$$

and calculate the temperature difference like previously shown in 26:

$$\Delta T_{theoretical,P} = \frac{q\,L}{Nu\,k} = 18.8K \tag{55}$$

Again we find a slight overestimate over the experimental value, showing that this also scales well with varying power density.

4 Compressed air cooling

A different idea from the previous approach, where air is freely streaming between the detector layers, is to include a tube in the stave which will then supply compressed cooling air directly to each PCB via orifices. We have to note that this would have the disadvantage of additional parts inside the detector.

4.1 Theory of compressible flow

To properly describe the flow through high pressure orifices we need to introduce the basics of compressible flow. At low speeds, the density of a fluid can be assumed as constant. This becomes untrue once the fluid approaches the speed of sound , which is the case at the orifices of our pressurized pipe. Now, compressibility effects have to be considered. We will assume the processes in the flow to be isentropic. Isentropic processes in a flow are adiabatic (meaning no heat is transfered) and reversible (meaning there is no dissipation of energy).

We need to introduce the dimensionless Mach number M, which is defined as the ratio of the speed of the flow u to the speed of sound a:

$$M = \frac{u}{a} \tag{56}$$

The speed of sound is the transmission speed of a disturbance through a fluid and can be calculated with:

$$a = \sqrt{\gamma R T} \tag{57}$$

where T is the fluid temperature, R is the specific gas constant ($\approx$ 287 J/(kg K) for air) and γ is the adiabatic index $\gamma = \frac{c_p}{c_V} = 1.4$ for air at standard temperature/pressure (and for the conditions of this experiment).

As a gas is forced through a duct with varying cross section A, its fluid properties change. The point of reference hereby is the so called stagnation point, where the velocity is zero. The duct is described as a converging or diverging nozzle (often times both: a converging diverging nozzle).

In a converging part of a nozzle, the fluid accelerates as pressure energy is converted into kinetic energy, which corresponds to the pressure decrease. Once the narrowest part of the nozzle, which is called the throat with an area of A*, is reached, there are two possibilities for the following diverging section. If the speed at the throat is less then $M = 1$, the pressure will increase again, while the velocity decreases (case B,C in the graphic). If the flow reaches sonic speed at the throat, the velocity further increases in the diverging section and the flow becomes supersonic ($M > 1$), while the pressure decreases (case D in the graphic).
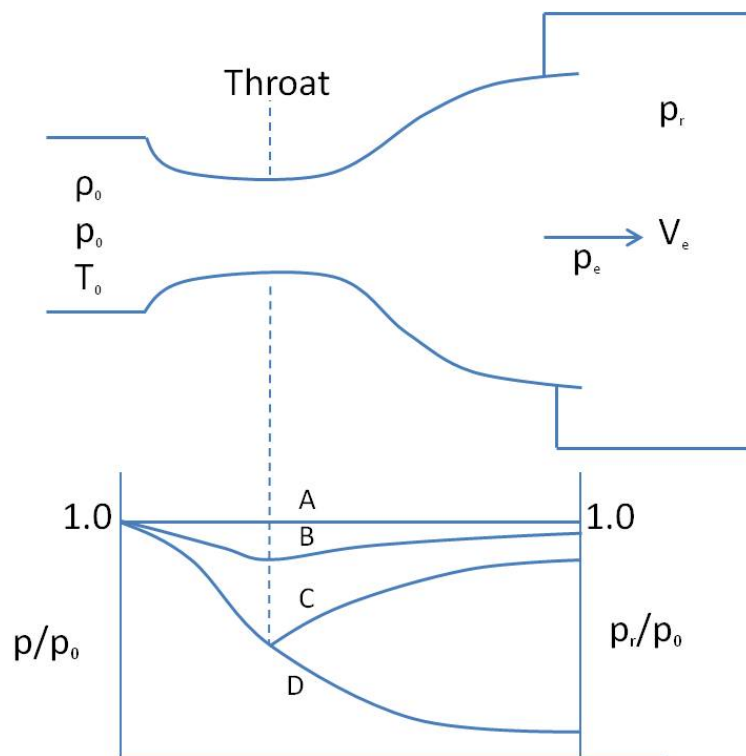

Figure 46: Converging diverging nozzle: pressure along the nozzle for different cases: B - subsonic flow throughout the nozzle; C - the flow reaches just below M=1 at the throat and then decelerates; D - the flow reaches M=1 at the throat and gets supersonic in the diverging section [11]

Isentropic flow relations

Those following equations describe the relation between properties of a fluid flow as it undergoes isentropic processes. ϕ_0 is representative for the initial quantity of the fluid at the stagnation point, ϕ is representative for the new quantity after the process [13].

Isentropic pressure relation:

$$\frac{p_0}{p} = \left(1 + \frac{\gamma - 1}{2}M^2\right)^{\frac{\gamma}{\gamma-1}} \tag{58}$$

Isentropic density relation:

$$\frac{\rho_0}{\rho} = \left(1 + \frac{\gamma - 1}{2}M^2\right)^{\frac{1}{\gamma-1}} \tag{59}$$

Isentropic temperature relation:

$$\frac{T_0}{T} = 1 + \frac{\gamma - 1}{2}M^2 \tag{60}$$

Also:

$$\frac{p_0}{p} = \left(\frac{\rho_0}{\rho}\right)^{\gamma} = \left(\frac{T_0}{T}\right)^{\frac{\gamma}{\gamma-1}} \tag{61}$$

We now can derivate the mass flow rate for an ideal compressible gas from this:

$$\dot{m} = \rho u A = \frac{A p_T}{\sqrt{T_0}}\sqrt{\frac{\gamma}{R}}M\left(1 + \frac{\gamma - 1}{2}M^2\right)^{-\frac{\gamma+1}{2(\gamma-1)}} \tag{62}$$

where p_T is the total pressure (pressure difference between up- and downstream). The mass flow rate reaches a maximum at $M = 1$. The flow is now described as choked and the mass flow rate is [15]:

$$\dot{m} = \frac{A p_T}{\sqrt{T_0}}\sqrt{\frac{\gamma}{R}}\left(\frac{\gamma + 1}{2}\right)^{-\frac{\gamma+1}{2(\gamma-1)}} \tag{63}$$

Flow inside the pressure pipe

Inside the pressure pipe the flow is comparably slow and can be assumed as

incompressible. The Darcy-Weisbach [12] equation can be used here to calculate
the pressure drop inside the pipe:

$$\Delta p = \frac{8lf\rho}{\pi^2 d^5} Q^2 \tag{64}$$

where Q is the volumetric flow, l and d the length and diameter of the pipe. f is
known as the friction factor and for turbulent flow it can be determined with the
help of Moody's chart.
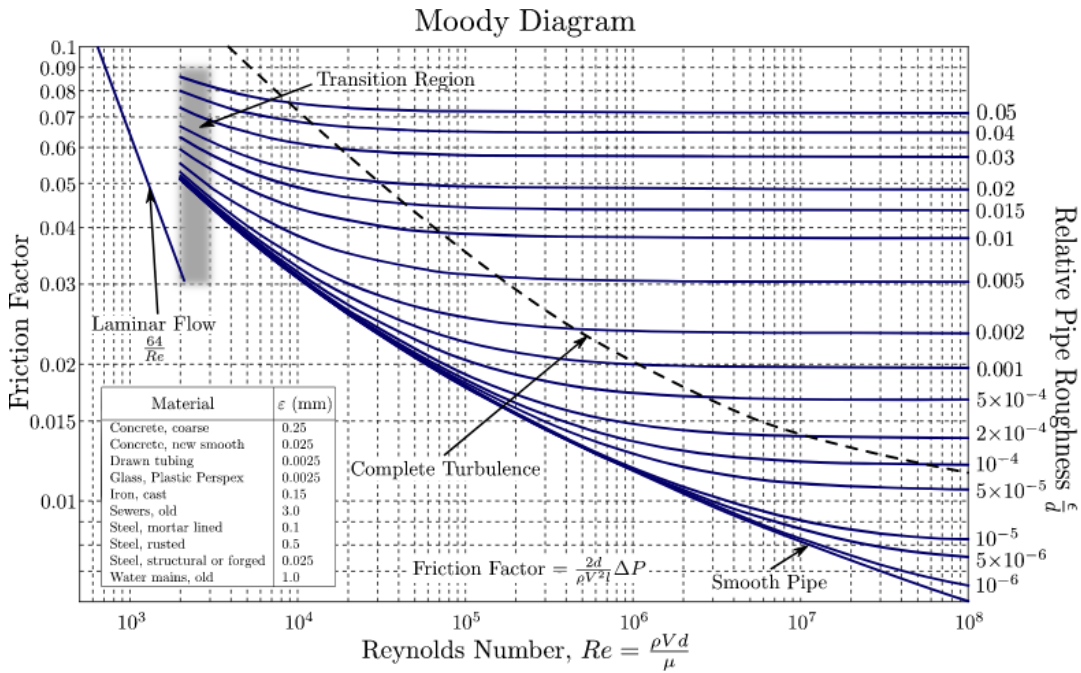
Figure 47: Moody's chart [17]

4.2   Experiment

4.2.1   Setup

To best simulate such a structure, we choose a simple plastic pipe with the length
of the space frame and a 2 cm inner diameter, which can simply be placed inside
the space frame. We then drilled holes (1 mm diameter) into the pipe, alongside
the length of the PCBs, as outlets for the compressed air. There is one hole every
2 cm for 130 cm and they have an alternating offset of 45° to the orthogonal of
the PCB plane to supply the PCBs from left to right.
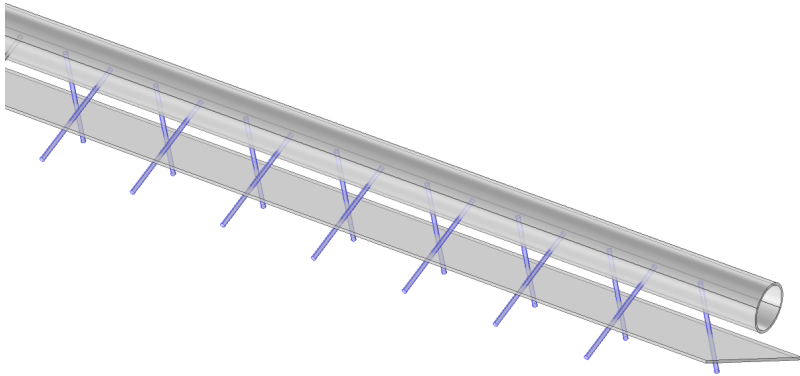
Figure 48: Schematic of the pressurized pipe over the stave, indicating the position and direction of the orifices through the blue colored lines

The setup includes a single stave mounted into the middle of the tube via the mounting brackets. Both ends of the pipe are then connected to pressurized air hoses, which themselves are connected to a variable compressed air supply. The first experiment was run with 2 bar air pressure, the second with 4 bar.

Figure 49: Setup of the compressed air cooling experiment

With the start of each experiment the air pressure was switched on as well as the heating. power. The temperature readout ran for 600s. The room temperature was 22.6 °C. The power output of the stave was 29.9 W.

4.2.2 Theoretical expectations

To calculate the total mass flow out of our pressurized pipe directly, we would need to know the pressure drop at every orifice. Since we cannot calculate this without in turn knowing the mass flow rate through the pipe, this presents us with a problem. To solve this, we will estimate a constant pressure inside the pipe, calculate the mass flow rate and then show why this was a good estimate.
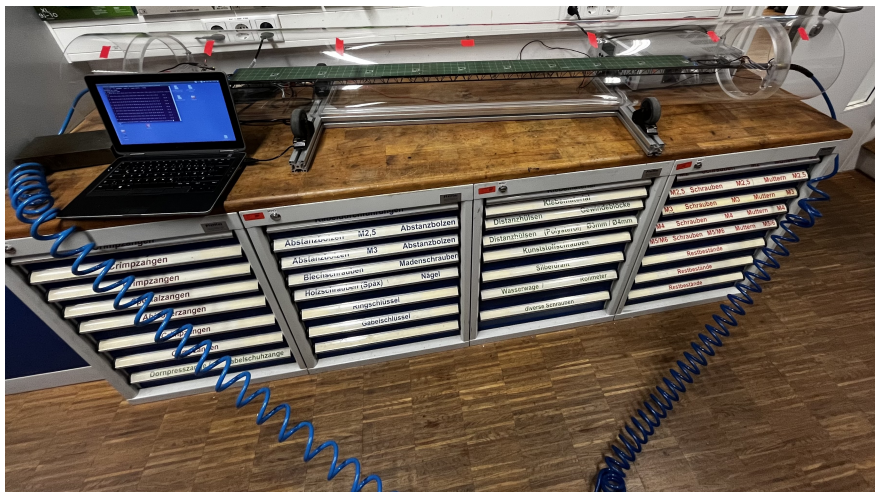
2 bar air pressure

Using equation 58 and 1 bar as the ambient pressure we calculate the Mach number:

$$\frac{p_0}{p} = \frac{3bar}{1bar} = \frac{1}{3} \qquad \Rightarrow \qquad M = 1.36 > 1 \qquad (65)$$

This means that the flow is choked, which is then also the case for 4 bar. We can now directly calculate the mass flow through one orifice (diameter 1mm) using equation 63:

$$\dot{m}_{orifice,2bar} = 0.369 g/s \qquad (66)$$

There are a total of 66 orifices across the pipe, but since both ends are connected to a pressure source, the relevant flow is that of 33:

$$\dot{m}_{2bar} = 33 \cdot m_{orifice,2bar} = 12.2 g/s \qquad (67)$$

With the density of air at 3 bar $\rho_0 = 3.5 kg/m^3$, we continue by calculating the volume flow (from left and right to the middle) inside the pressure pipe:

$$Q_{2bar} = \frac{\dot{m}}{\rho_0} = 0.0035 m^3/s \qquad (68)$$

and the velocity (diameter 0.02m)

$$u_{2bar} = Q/A = 11 m/s \qquad (69)$$

to determine the Reynolds number inside the pressurized pipe:

$$Re_{2bar} = 42000 \qquad (70)$$

We further calculate the relative pipe roughness:

$$\frac{\epsilon}{d} = \frac{0.0025mm}{20mm} = 1.25 * 10^{-4} \tag{71}$$

Now we can use Moody's chart to estimate a friction factor of

$$f_{2bar} = 0.022 \tag{72}$$

To determine the pressure loss we use equation 64 and insert our results. The pipe length from one side of the pipe to the middle is $l = 1m$.

$$\Delta p = \frac{8lf\rho}{\pi^2 d^5}Q^2 = 240Pa \tag{73}$$

This is actually an overestimation, since the volumetric flow decreases towards the middle as air exits the orifices. So we can safely say that there is no significant pressure drop along the pipe and our original approximation of a constant pressure inside the pipe holds true.

4 bar air pressure

I will just list the results of this setup, since the process is the same. Though we have to note that $\rho_0 = 5.9kg/m^3$ and the absolute pressure here is 5 bar:

$$\dot{m}_{orifice,4bar} = 0.738g/s \tag{74}$$

$$\dot{m}_{4bar} = 33 \cdot m_{orifice,4bar} = 24.4g/s \tag{75}$$

$$Q_{4bar} = \frac{\dot{m}}{\rho_0} = 0.0041m^3/s \tag{76}$$

$$u_{4bar} = Q/A = 13m/s \tag{77}$$

$$Re_{4bar} = 83000 \tag{78}$$

$$f_{4bar} = 0.014 \tag{79}$$

$$\Delta p_{2bar} = \frac{8lf\rho}{\pi^2 d^5}Q^2 = 350Pa \tag{80}$$

4.2.3 Results

Both temperature distributions are quite irregular due to some sensors being directly in the air jet and others not. The temperature for both setups slightly falls from left to right. This is probably due to the pressurized air hoses not being of the exact same type. We have shown before that there is no pressure drop towards the middle of the pipe and so there is also no temperature increase towards the middle of the pipe as expected.

Since the distribution is so irregular, we are taking an average over the full distribution instead of trying to find the plateau temperature noting that we cannot directly compare these to the previous experiments.

Figure 50: 2 bar: temperature distribution plot after 10 minutes (input temp.: 22.6 °C), x-axis corresponds to the x position on the PCBs, one plotted line for each y-position on the PCBs, vertical lines to mark PCB transitions

We get an average temperature of $T_{average,2bar} = 26.4$ °C, and therefore:
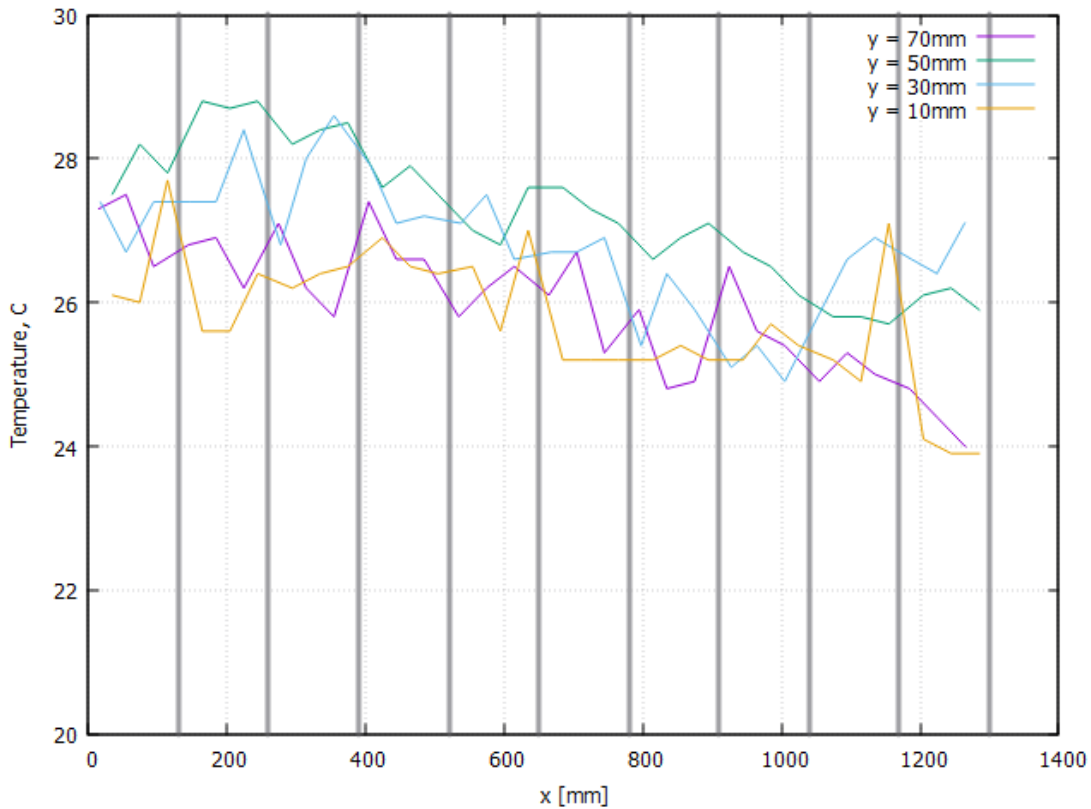
$$\Delta T_{2bar} = 3.5K \tag{81}$$
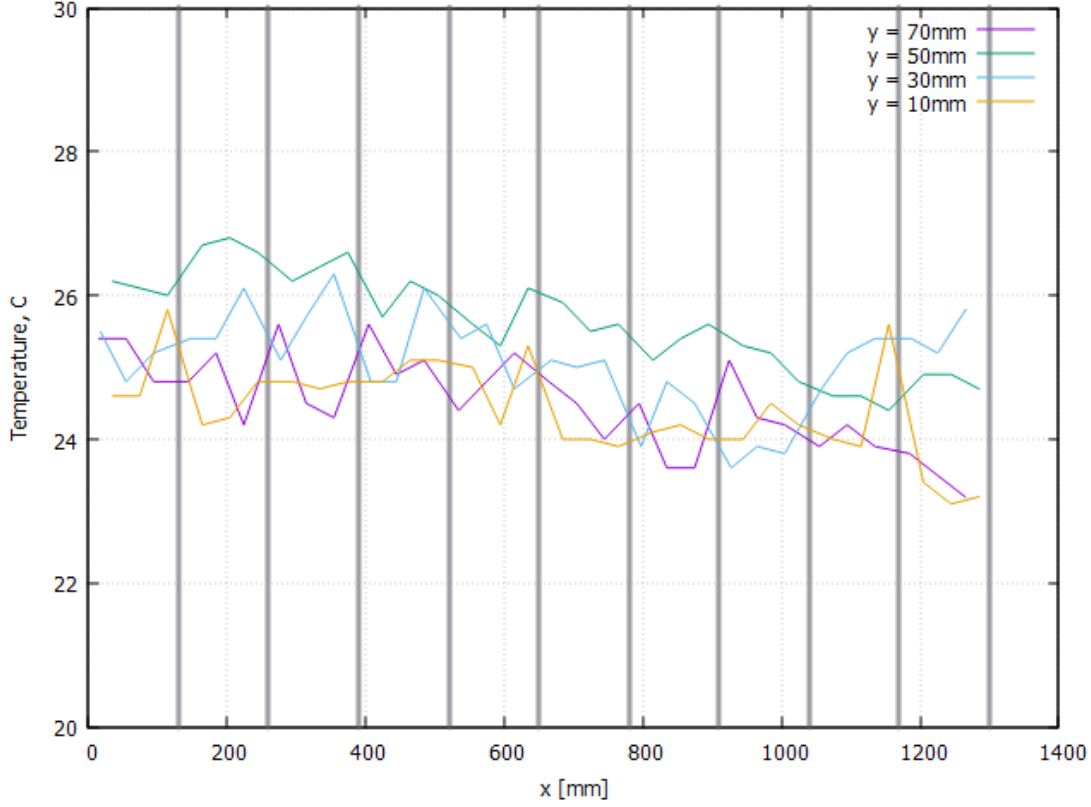
Figure 51: 4 bar: temperature distribution plot after 10 minutes (input temp.: 22.6 °C), x-axis corresponds to the x position on the PCBs, one plotted line for each y-position on the PCBs, vertical lines to mark PCB transitions

We get an average temperature of $T_{average,2bar} = 24.9$ °C, and therefore:

$$\Delta T_{2bar} = 2.3K \tag{82}$$

Summarizing we can say, that cooling with compressed air works extremely well, achieving temperatures only a few degrees over room temperature. To compare the mass flow to that of previous experiments with uncompressed air we have to double $\dot{m}_{4bar}$ (to account for all 66 orifices) and get:

$$\dot{m}_{4bar,total} = 0.049 kg/s \tag{83}$$

Using the experiment from chapter 3.9.4 (50% duty cycle) as point of comparison

$$\dot{m} = \rho_{1bar} u_{average} A = 0.136 kg/s \tag{84}$$

we find that cooling with pressurized air performs much better with an even lower air flow. This obviously stems from directly supplying fresh cooling air to the PCBs. The cost of implementing such a method is the need to include pressure pipes inside the detector.

We also note that for a real life scenario, the pressurized structure used (pipe) should be tuned to supply air more evenly to achieve a less irregular distribution. This could be done by tuning the position and number of exit holes of the pipe.

5 CFD simulations

This chapter includes an introduction into the theory of computational fluid dynamics (CFD) and the results of a number of simulations of the experimental setup of chapter 3.9.4 using the simulation platform COMSOL Multiphysics.

5.1 Theory of turbulence modeling

Computational fluid dynamics is a vast topic and impossible to fully capture in the scope of this thesis. This section is achieving to cover the basics of turbulent flow modeling on the basis of the Reynolds-Averaged Navier-Stokes equations and its solving models. This section is based on the books [1] and [3] as well as insights from the websites [9] and [7].

5.1.1 Reynolds-Averaged Navier-Stokes equations RANS

In this section I will make use of the Einstein notation. We will limit the scope of this introduction to incompressible flows $\rho = const.$.

Starting off with the Navier-Stokes equation (momentum conservation)

$$\frac{\partial u_i(\boldsymbol{x},t)}{\partial t} + u_j(\boldsymbol{x},t)\frac{\partial u_i(\boldsymbol{x},t)}{\partial x_j} = -\frac{1}{\rho}\frac{\partial p(\boldsymbol{x},t)}{\partial x_i} + \nu\frac{\partial^2 u_i(\boldsymbol{x},t)}{\partial x_j \partial x_j} \tag{85}$$

which describe viscous fluids in terms of instantaneous quantities $\phi_i(\boldsymbol{x},t)$, which are time and space dependent. A quick explanation of the terms:

$\frac{\partial u_i(\boldsymbol{x},t)}{\partial t}$ is the rate of change of velocity with respect to time. $u_j(\boldsymbol{x},t)\frac{\partial u_i(\boldsymbol{x},t)}{\partial x_j}$ is the convective term describing how the velocity component u_j contributes to the rate of change of the velocity component. $-\frac{1}{\rho}\frac{\partial p(\boldsymbol{x},t)}{\partial x_i}$ is simply the pressure gradient.

$\nu \frac{\partial^2 u_i(\boldsymbol{x},t)}{\partial x_j \partial x_j}$ is the term describing effects due to the viscosity $\nu = \mu/\rho$ of the fluid via the rate of change of the velocity gradients, which are the Laplacian of u_i.

We also use the equation of mass conservation:

$$\frac{\partial u_i(\boldsymbol{x},t)}{\partial x_i} = 0 \tag{86}$$

Reynolds averaging

The idea of Reynolds averaging is that we can decompose the flow quantities $\phi(\boldsymbol{x},t)$ into a time averaged part $\overline{\phi(\boldsymbol{x})}$ plus a time dependent fluctuating part $\phi'(\boldsymbol{x},t)$:

$$\phi_i(\boldsymbol{x},t) = \overline{\phi_i}(\boldsymbol{x}) + \phi_i'(\boldsymbol{x},t) \tag{87}$$

with

$$\overline{\phi_i}(\boldsymbol{x}) = lim_{T\to\infty} \frac{1}{T} \int_0^T \phi_i(\boldsymbol{x},t)dt$$

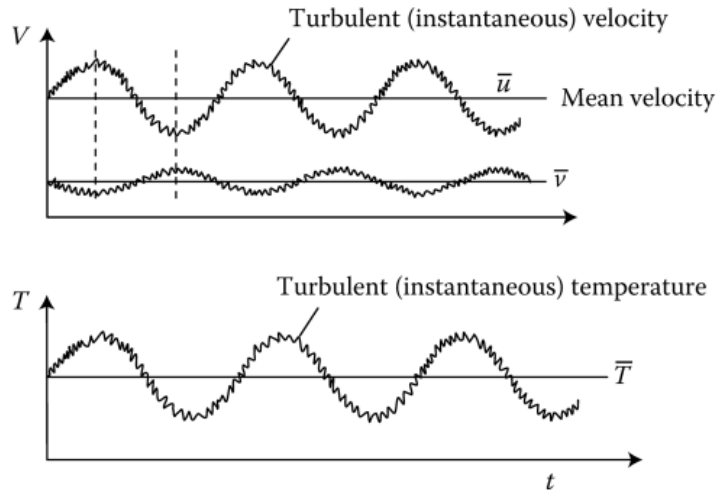$$0 = lim_{T\to\infty} \frac{1}{T} \int_0^T \phi_i'(\boldsymbol{x},t)dt$$

Figure 52: Instantaneous time-dependent velocity and temperature profiles inside a turbulent boundary layer, [3]

It is important to note that while $\overline{\phi_i'} = 0$, this is not the case in $\overline{\phi_i'\phi_j'} \neq 0$. We can now substitute these into the Navier-Stokes equations 85 and 86 and take the

time average to get the Reynolds-averaged Navier-Stokes equations.(This is not trivial, an example for a derivation can be found in [3].)

Mass conservation:

$$\frac{\partial \overline{u}_i}{\partial x_i} = 0 \tag{88}$$

and momentum conservation:

$$\overline{u}_j(\boldsymbol{x})\rho\frac{\partial \overline{u}_i(\boldsymbol{x})}{\partial x_j} = -\frac{\partial \overline{p}(\boldsymbol{x})}{\partial x_i} + \frac{\partial}{\partial x_j}\left[\left(\mu\frac{\partial \overline{u}_i(\boldsymbol{x})}{\partial x_j} + \frac{\partial \overline{u}_j(\boldsymbol{x})}{\partial x_i}\right) - \rho\overline{u'_j(\boldsymbol{x},t)u'_i(\boldsymbol{x},t)}\right] \tag{89}$$

We now managed to write an equation that almost only contains time independent mean quantities $\overline{\phi(\boldsymbol{x})}$, with the exception of the $\rho\overline{u'_j u'_i}$ expression. This is known as the Reynolds stress term τ_{ij} and it basically describes turbulent fluctuations. This term prohibits us from directly solving the equation for $\overline{u}_i$. This is known as the turbulence closure problem. To overcome this, we have to estimate the term.

5.1.2 Eddy viscosity modeling

Modeling the Reynolds stress term is subject of this chapter. It is important to note that this is always only an approximation that comes with loss of information and not an exact evaluation.

The assumption of eddy viscosity modeling is that the turbulent fluctuations are analogous to the random Brownian motion of particles. This random motion of particles can transport momentum along the velocity gradient $\partial \overline{u}_x/\partial y$ (in one dimension):

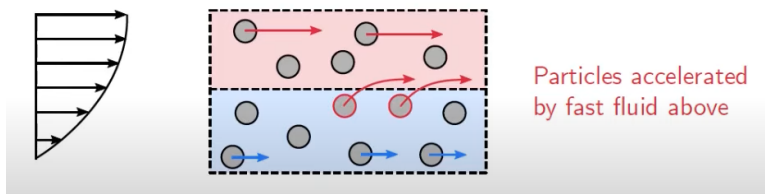$$-\rho\overline{u'_x u'_y} = \mu_T\frac{\partial \overline{u}_x}{\partial y} \tag{90}$$

Figure 53: transfer of momentum through particle interactions [19]

This is known as the Boussinesq hypothesis. μ_T is the eddy viscosity and is a measure of the strength of the diffusion of momentum. From this the total

equation for the Reynolds stress term can be derived:

$$-\rho\overline{u_i'u_j'} = \mu_T\left(\frac{\partial \overline{u}_i}{\partial x_j} + \frac{\partial \overline{u}_j}{\partial x_i} - \frac{1}{3}\frac{\partial \overline{u}_k}{\partial x_k}\delta_{ij}\right) - \frac{2}{3}\rho k\delta_{ij} \qquad (91)$$

δ_{ij} is the kronecker delta which adds necessary terms of correction for the normal stresses $(-\rho\overline{u_i'u_i'})$. k here is the turbulent kinetic energy:

$$k = \frac{1}{2}\overline{u_i'u_i'} \qquad (92)$$

We now shifted the problem of solving the Reynolds stress to solving for the eddy viscosity μ_T. In CFD programs there usually is a variety of models to choose from to do so. The easiest approach is to use a mixing length l_m, which is an indicative size of the eddys that exist in the flow. The Prandtl mixing length hypothesis says that the size of the eddys is limited by the presence of walls, the further the distance from the wall (y), the larger eddies can exist in the flow. They are related by:

$$l_m = \kappa y \qquad (93)$$

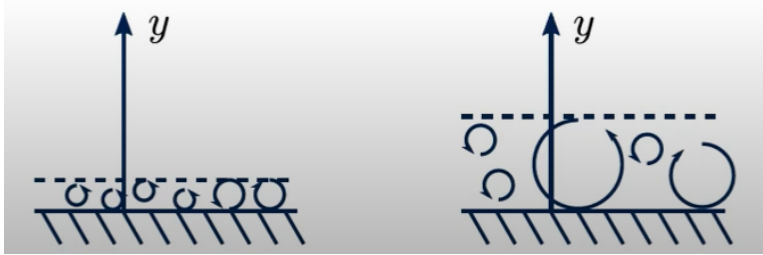where κ is a simple experimental constant.

Figure 54: Relation between wall distance and eddy size [19]

The size of the eddys is obviously and indicator of the strength of the turbulence in the flow. We can now simply relate the mixing length to the eddy viscosity:

$$\mu_T = \rho k^{1/2}l_m \qquad (94)$$

$k - \epsilon$-model

One of the most popular models to model the eddy viscosity and the one I used

with COMSOL Multiphysics is the $k - \epsilon$-model. In the $k - \epsilon$-model, instead of algebraically estimating a mixing length, two new partial differential equations are solved within the boundaries of the problem to calculate μ_T. The transport equation for the turbulent kinetic energy k is:

$$\rho\frac{\partial k}{\partial t} + \rho\mathbf{u} \cdot \nabla k = \nabla \cdot \left(\left(\mu + \frac{\mu_t}{\sigma_k}\right)\nabla k\right) + P_k - \rho\epsilon \tag{95}$$

And one for the dissipation rate ϵ:

$$\rho\frac{\partial \epsilon}{\partial t} + \rho\mathbf{u} \cdot \nabla \epsilon = \nabla \cdot \left(\left(\mu + \frac{\mu_t}{\sigma_\epsilon}\right)\nabla \epsilon\right) + C_{\epsilon 1}\frac{\epsilon}{k}P_k - C_{\epsilon 2}\rho\frac{\epsilon^2}{k} \tag{96}$$

The production term P_k reads:

$$P_k = \mu_T\left(\nabla\mathbf{u} : \left(\nabla\mathbf{u} + (\nabla\mathbf{u})^T\right) - \frac{2}{3}\left(\nabla \cdot \mathbf{u}\right)^2\right) - \frac{2}{3}\rho k\nabla \cdot \mathbf{u} \tag{97}$$

The eddy viscosity is then calculated with:

$$\mu_T = C_\mu\frac{\rho k^2}{\epsilon} \tag{98}$$

$C_\mu = 0.09$, $C_{\epsilon 1} = 1.44$, $C_{\epsilon 2} = 1.92$, $\sigma_k = 1.0$ and $\sigma_\epsilon = 1.3$ are experimentally determined constants. The constants and transport equations are taken from the COMSOL documentation [8].

With the eddy viscosity now modeled, the RANS equations can finally be solved for the average velocity $\overline{u}_i$.

I would like to note that while the $k - \epsilon$-model produces more accurate solutions than algebraic models, I usually simulated problems with an algebraic model first before using its solution as initial conditions for the iteration of the $k - \epsilon$-model. This is really helpful to cut computation times since the $k - \epsilon$-model is computationally much more expensive than algebraic models.

5.2   Simulations with COMSOL Multiphysics

COMSOL Multiphysics is a simulation platform that provides fully coupled multiphysics capabilities [10], meaning it is able to computationally solve partial

differential equations from different areas of physics. In this case those areas are fluid dynamics and heat transfer. COMSOL numerically solves PDEs via the finite element method [21]. This places a mesh over the geometry of the problem that discretizes it into finite elements. Each element can then described by simple equations which are combined to a larger system of equations which are then solved numerically.

Simulating a problem starts with defining its geometry and material properties. After that the suitable physics interface has to be chosen and the initial conditions have to be defined. The third and final step before the computation can be started is defining a mesh over the full geometry.

Before we go into the results of the different simulations, I will specify the general setup of all simulations. I chose the conditions and results of the experiment 3.9.4 (50% duty cycle) as a basis, so the average inlet velocity is set as 2.5 m/s, the inlet air temperature as 23.7 °C and the total power output of the stave as 31.3 W. I modeled all simulations in 2D since it is a good approximation (which we have shown in experiment 3.6) and computationally much cheaper (computation times upward of 10 min are were still common for the more complex geometries). The basic 2D geometry is really simple: the air duct with the length and height (diameter) of the tube plus the stave length times its height in the middle of the tube. The material of the PCBs is FR4, which has predefined material properties, including a thermal conductivity of ($k_{FR4} = 0.2$ W/(mK)). This not fully correct, since the PCBs also have to layers of 35 μm copper, which has a much higher thermal conductivity ($k_{copper} = 401$ W/(mK)). We take a weighted sum of the thermal conductivities to get:

$$k_{total} = \frac{k_{FR4} * 70\mu m \ + \ k_{copper} * 730\mu m}{800\mu m} = 35.3 W/(mK) \tag{99}$$

All simulations were run as stationary studies, meaning they solved for a static temperature and velocity distribution.

5.2.1 Nonuniform heat flux

This part includes the comparison of two models: The first is the simple modeling of the stave as a flat plate with a thickness equal to that of the PCBs and a uniform surface heat flux. In the second model, I included the missing heating coil parts by including "non heating power producing areas" in the geometry.
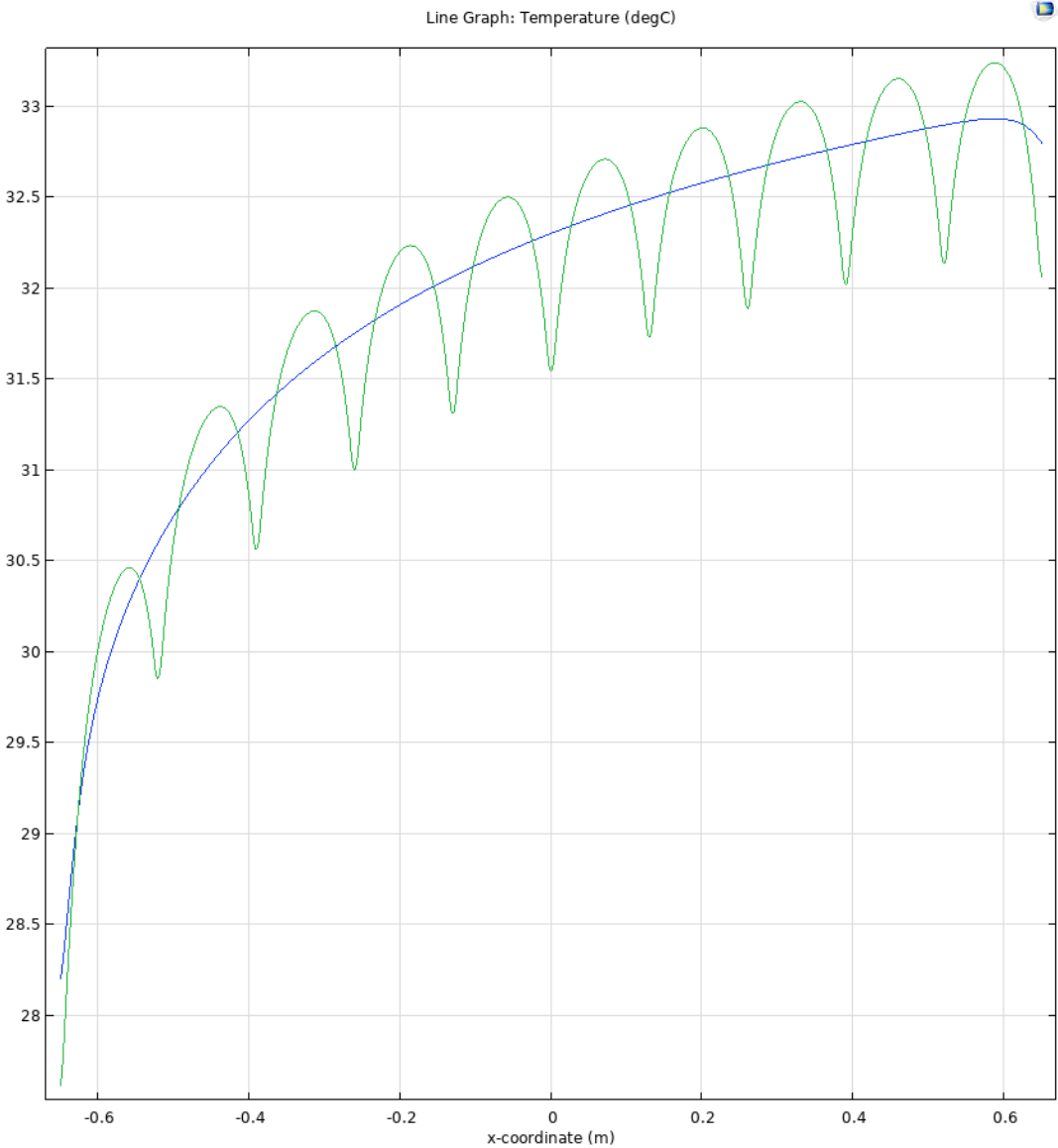

Figure 55: Surface temperature of the stave, blue for the flat plate simulation, green for the nonuniform heat flux simulation

The characteristic jagged structure of previous temperature distributions becomes visible as expected. The overall cooling performance remains unchanged.

5.2.2 Flat plate versus uneven surface

In this model, I tried to represent the uneven lower side of the stave with its space frame. Modeling the full space frame is computationally much too expensive (in 2D also not geometrically realizable). To simulate a disturbance in the airflow I simply added interior walls with a height of 5 mm at every PCB intersection.
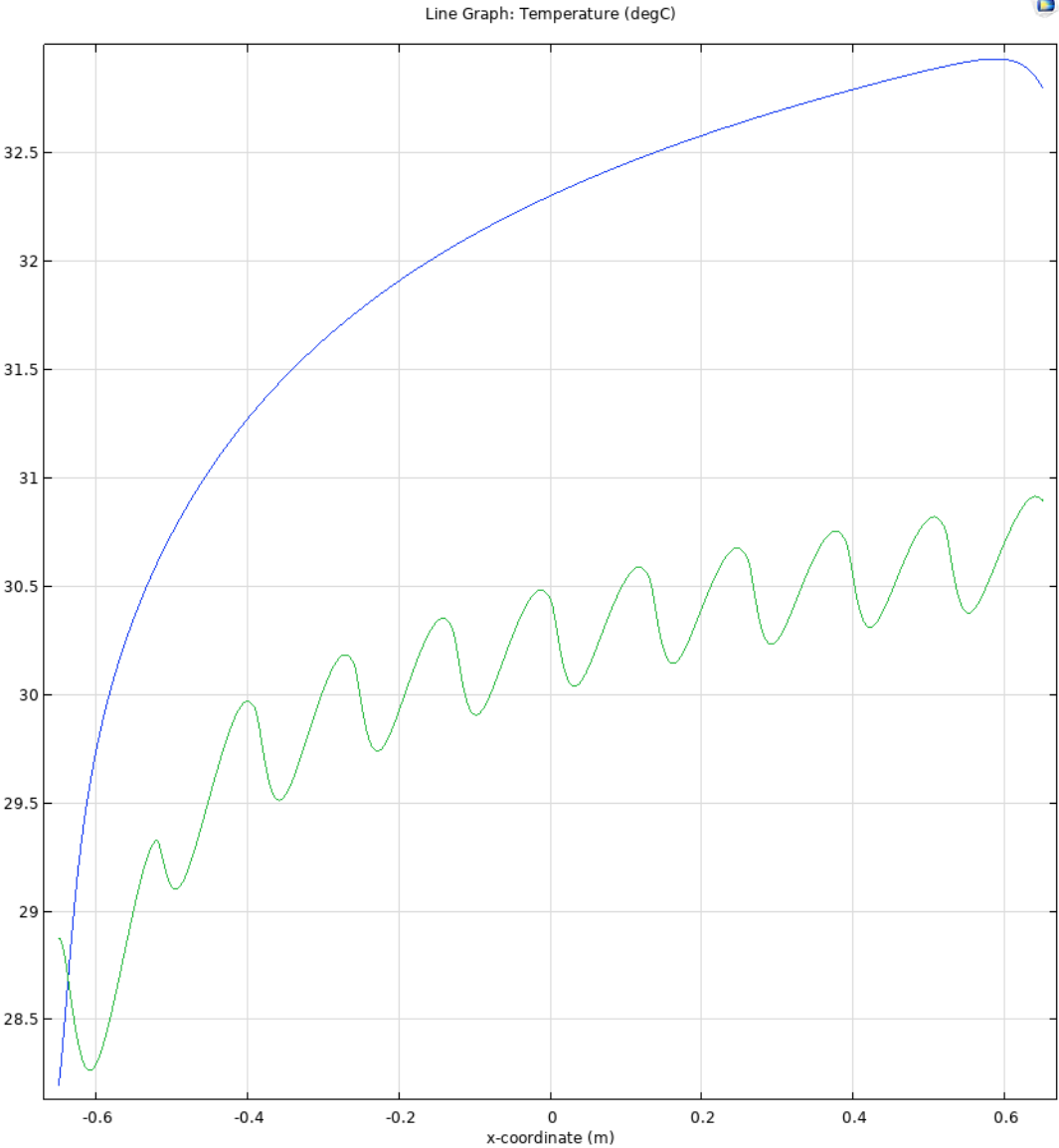

Figure 56: Surface temperature of the stave, blue for the flat plate simulation, green for the uneven "space frame side"
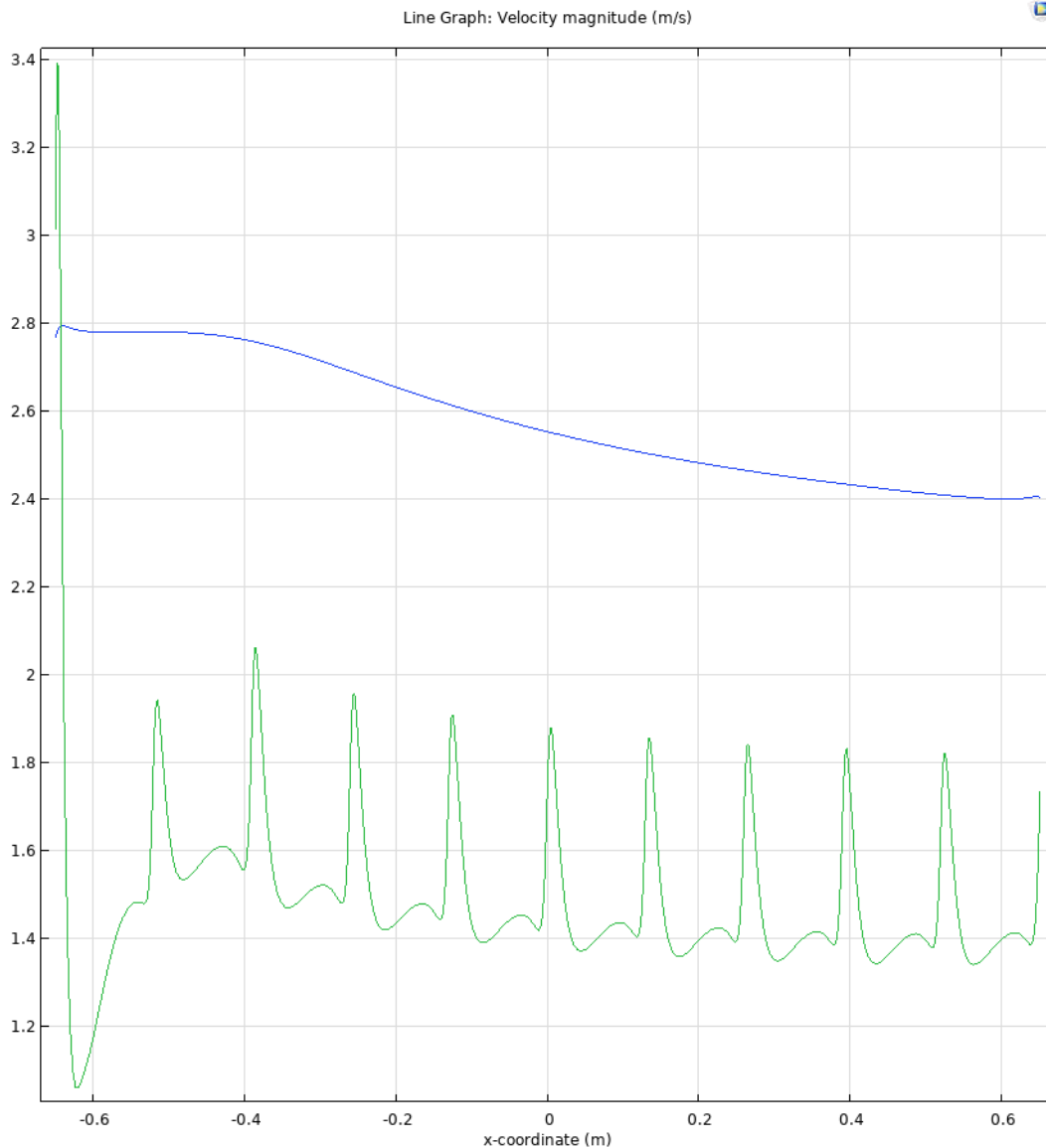
Figure 57: Fluid velocity 1 cm over the surface, blue for the flat plate simulation, green for the uneven "space frame side"

One can see that the space frame side with its uneven side has a slightly better cooling performance than the simple flat plate even though the fluid velocity on this side is much lower due to the "obstacles" in the flow. Testing varying interior wall heights shows that the cooling performance increases with the wall height. In the experimental test 3.7 we have seen almost no difference in cooling performance between air flow only on the flat side and only on the space frame side, but we can clearly see that the extra turbulence created by tripping the flow with obstacles results in a better cooling performance even at the expense

of a lower fluid velocity. This further shows why our theoretical estimations via formula 14 produce slightly higher temperatures than experimentally measured - the calculations underestimate the turbulence and therefore Reynolds number.

5.2.3 Final model

We have shown the effects of an uneven surface and power density. The task is now to simulate a realistic model which will be close to the experiment 3.9.4 (50% duty cycle). The geometry of the final setup includes the uneven power density, one side will be a flat surface and on the other side we will feature the previous described interior walls. Since the interior wall height is a representative parameter of the obstruction caused by the space frame I ran multiple simulations with varying heights to best fit the temperature distribution to the experimental plateau region.

The found representative height is:

$$h \approx 10mm \tag{100}$$

We can actually understand this parameter to be a sort of characteristic length of the space frame in 2D.
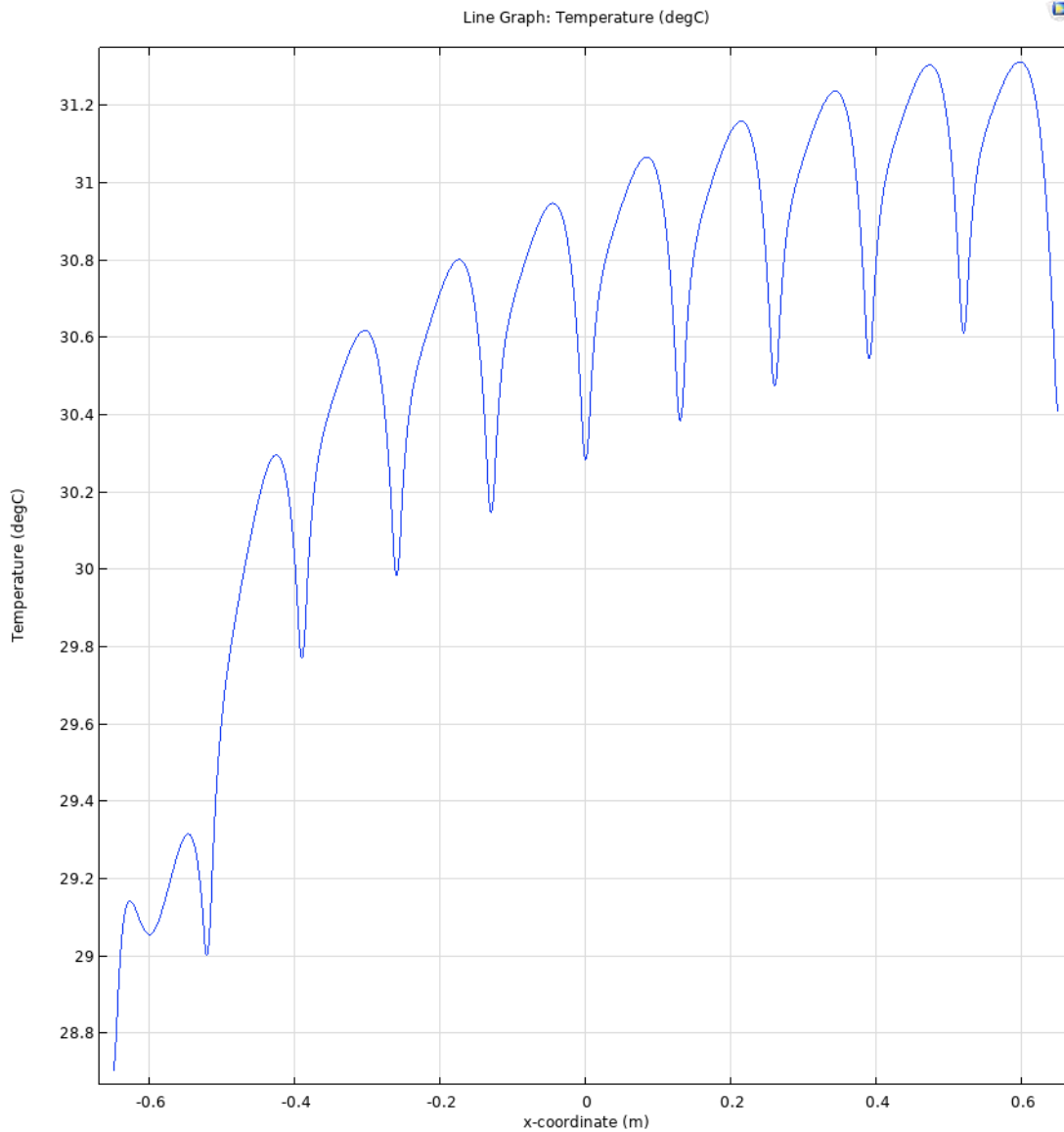
Figure 58: Surface temperature of the final simulation

Exporting the data in form of a table, we can plot this distribution next to the one from experiment 3.9.4 (50% duty cycle):
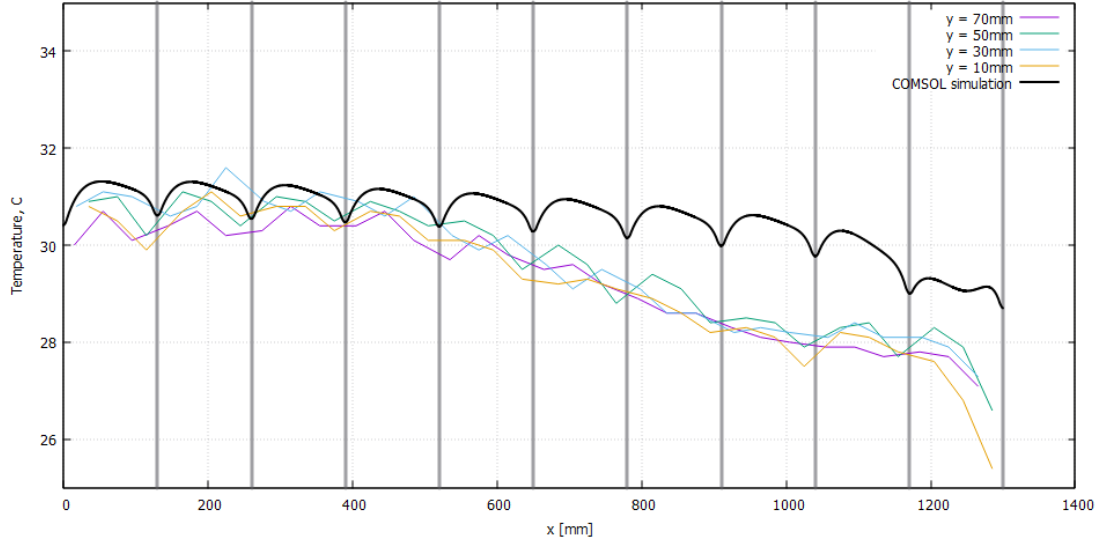
Figure 59: Surface temperature of the simulation versus the distribution of experiment 3.9.4 (50% duty cycle)

With the plateau regions now matching perfectly, the only remaining difference is the entrance region with a still small maximum temperature difference of approximately 2 K. This has to be the result of a different entrance length (length before the flow is fully developed). A strong decrease in entrance length is a common phenomenon of tripped flows (posing an obstacle at the start entrance), which is obviously the case here. We would still expect this effect to be similar to the experiment since also there the flow is tripped through the space frame. All we can comment on this is that the interior walls used in this simulation are not a perfect representation of the space frame geometry, which leads to the flow being "tripped differently". We can conclude this part by saying that this simulation is still as close as we can get to the experiment without drastically increasing computation power or time and that it does provide a near perfect result for the fully developed plateau region.

5.2.4 Impact of no radiation

Since in the final ALICE 3 detector there will be no heat dissipation via radiation (the ambient temperature is that of the next barrel layer), we are making a final simulation equal to the previous one, but not including the physics interface for radiation.
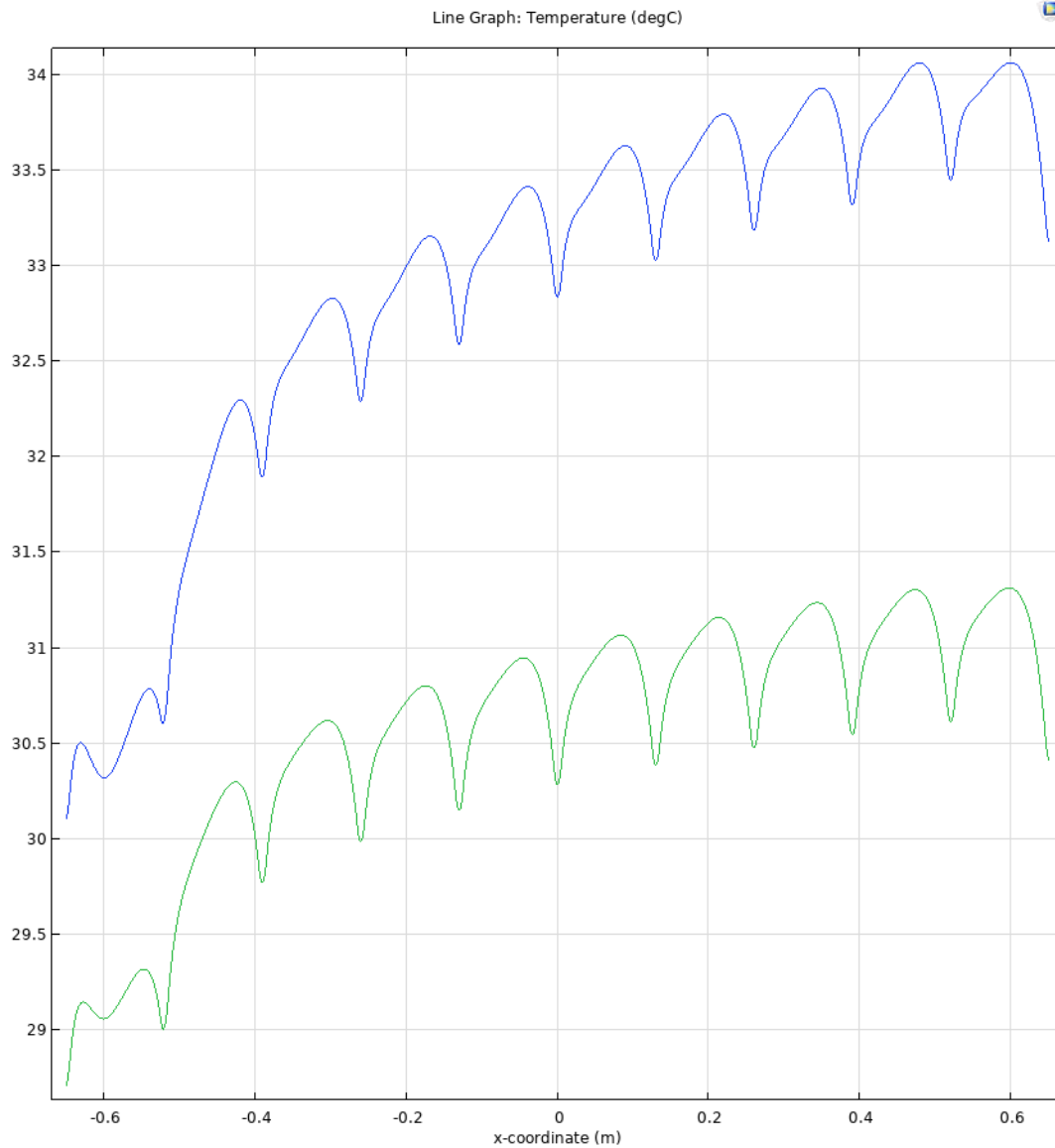
Figure 60: Surface temperature of the final simulation (green) versus without including heat dissipation by radiation (blue)

The plateau temperature difference is about 4 K, which is about the rise of temperature expected when not considering radiation in our analytical theory. This is our best estimate for the real conditions in the ALICE 3 detector for given input conditions.

6 Discussion

6.1 Scalability of the Nusselt number model calculations

The goal of this thesis was to to build a model of reference to predict the requirements and parameters necessary for effective air cooling of the outer three layers of the outer tracker detector. We will start by analysing the accuracy of our Nusselt number model (based on equation 14) calculations of the varying conditions in chapters 3.9 and 3.10. Here is an overview:

20% duty cycle:	Re=20000	ΔT_{exp}=11.9 K	ΔT_{theo}=12.9 K
50% duty cycle:	Re=39000	ΔT_{exp}=7.1 K	ΔT_{theo}=10.3 K
100% duty cycle:	Re=71000	ΔT_{exp}=4.8 K	ΔT_{theo}=7.3 K
doubled power:	Re=39000	ΔT_{exp}=15.1 K	ΔT_{theo}=18.8 K

The theoretical estimates are consistently larger than the experimental results by a few degrees. As we have shown this is not a failure of the model, but an underestimation of the Reynolds number. While the results are not very accurate, they do scale well with a variation of input conditions both in heating power and air speed, consistently producing a slight overestimate. Therefore this will provide a good estimate of an upper limit of the plateau temperature of the required input conditions for the final detector.

In all setups we have seen that the fully developed flow and its corresponding plateau temperature is reached after about two thirds of the stave. We have seen and shown via calculation (in chapter 3.4.3) that the temperature does not significantly increase in the fully developed region. Since it is this maximum plateau temperature that is of interest for the detector we can safely conclude, that there is no reason not to cool the full 264 cm of barrel length continually instead of laying an extra air supply at their middle separation, which would have increased the complexity of the air cooling supply, since there will be very limited space between the left and right barrel part.

6.2 Other air cooling strategies

We also analyzed two different strategies of air cooling. By far the best performing was cooling by compressed air (chapter 4). This approach outperforms the non

compressed air methods by a big margin, producing results only a few degrees over ambient temperature. The problem with this approach is that it comes with similar disadvantages as water cooling: the need of a pressure pipe installation inside the detector plus a supply of oil free compressed air is not only more expensive than the implementation of an unpressurized air flow, but also increases the material budget of the detector, worsening its performance.

While this approach becomes irrelevant if a "free flow" approach works, it would still be an improvement over the complexity of a leakless water cooling system, should the requirements of the detector chips not allow for a "free flow" approach.

We also tested a cross flow strategy (chapter 3.8) that would alternate the direction of inflow with neighbouring barrel layers. As we have shown this strategy works by overlapping the sections of the flow which are not fully developed, utilizing their increased heat transfer coefficient in their respective region. After the fully developed region is reached it does not increase cooling performance anymore.

If the choice would be to cool the full 264 cm continually this approach would be of no use, since the fully developed regions will not overlap in the middle anymore. We also cannot be sure that the entrance length of the final detector application will be same as in the experiment. We have seen that where and how the flow is tripped can have a big impact on the entrance length (as seen in the COMSOL simulations).

Regardless of these arguments, the alternating inflow will also increase the complexity of the air supply structure, which might not be worth the rather small increase in cooling performance. Summarizing we can say that while the cross flow strategy does theoretically provide slightly better cooling performance, it is unlikely to be useful in the final detector.

6.3   COMSOL simulation and final conclusion

We were able to produce a very accurate simulation of the experiment in the plateau region. There were inconsistencies in the entrance region in comparison to the experiment. This is however of lesser interest than the plateau region, so we can interpret this as a well working model of the problem. Given the vast

flexibilities of model building with COMSOL, we will be able to alter this final simulated model to our liking to further adjust to possible changes in conditions of the final detector. With more computational power we could further model 3D geometries and or multiple barrel layers at a time. This result with its fitted interior wall parameter of 1 cm can provide as a solid basis representing the simple geometry with a correct topology, meaning it results in a correct turbulence of the flow.

In the real ALICE 3 detector there will be no heat dissipation due to radiation as mentioned before. With both COMSOL and the Nusselt number model we can easily account for this.

Having two models on our hands which will scale well with altering input conditions to provide reliable results, we achieved the goal of this thesis.

A C++ Code

```cpp
#include <iostream>
#include <fstream>
#include <sstream>
#include <vector>


int main() {

    // Open the input file
    std::ifstream inputfile("temperature.txt");
    if (!inputfile.is_open()) {
        std::cerr << "Error opening input file\n";
        return 1;
    }


    // Open the output_board file for writing and truncate its content
    std::ofstream output_board("output_board.txt", std::ofstream::trunc);
    if (!output_board.is_open()) {
        std::cerr << "Error opening output_board file\n";
        return 1;
    }


    // Open the output_air file for writing and truncate its content
    std::ofstream output_air("output_air.txt", std::ofstream::trunc);
    if (!output_air.is_open()) {
        std::cerr << "Error opening output_air file\n";
        return 1;
    }


    // Open the output_line file for writing and truncate its content
    std::ofstream output_line("output_line.txt", std::ofstream::trunc);
    if (!output_line.is_open()) {
        std::cerr << "Error opening output_line file\n";
        return 1;
    }


    // Open the outputfile file for writing and truncate its content
    std::ofstream outputfile("outputfile.txt", std::ofstream::trunc);
    if (!outputfile.is_open()) {
        std::cerr << "Error opening outputfile file\n";
```

```cpp
        return 1;
    }


    // Open the coordinate file
    std::ifstream coordinates("coordinates.txt");
    if (!coordinates.is_open()) {
        std::cerr << "Error opening coordinates\n";
        return 1;
    }


    std::cout << "All files present\n";


    // Split the input into a vector
    std::vector<std::string> entries;
    std::string entry;
    while (inputfile >> entry) {
        entries.push_back(entry);
    }
    int steps = entries.size() / 162;


    // Rewrite board temperatures to vector
    std::vector<std::string> board;
    for (int i = 0; i < steps; i++){
        for (int j = 0; j < 10; j++){
            for (int k = 2; k < 14; k++){
                board.push_back(entries[i*162 + j*16 + k]);
            }
        }
    }


    /*
    // Averaging (commented out, since not used)

    double sum = 0.0;
```

```cpp
    // Sum up the first 120 entries
    for (size_t i = 0; i < 120; ++i) {
        sum += std::stod(board[i]); // Convert each string entry
        //to double for the sum
    }

    // Calculate the average
    double average = sum / 120;

    //Calculate differences
    std::vector<double> difference;
    for (int i = 0; i < 120; ++i) {
        difference.push_back(std::stod(board[i]) - average);
    }

    //Update values
    for (size_t i = 0; i < board.size(); i++) {
        double value = difference[i%120];
        board[i] = std::to_string(std::stod(board[i]) - value);


    }

    std::cout << "Averaging succesful\n";
    */




    // Rewrite air temperatures to vector
    std::vector<std::string> air;
    for (int i = 0; i < steps; i++){
        for (int j = 0; j < 10; j++){
            for (int k = 14; k < 18; k++){
                air.push_back(entries[i*162 + j*16 + k]);
            }
        }
    }
```

```cpp
// Rewrite entries in one column in the output_board file:
//this is just an interim step file, I thought I could
//maybe use this for something
for (const auto& e : board) {
    output_board << e << "\n";
}


// Rewrite to output_air file: this can be used to plot the air
//sensor temperature against X
for (size_t i = 0; i < air.size()/40; i++) {
    for (int j = 0; j < 40; j+=4){
        // Write the air entry with coordinates to the
        //output_air file
        output_air << j/4*130 << "\t" << air[i*40+j+1] << "\n";
    }
    output_air << "\n";
    output_air << "\n";


}




// Write coordinates into vectors and add empty entries
std::vector<std::string> Xcoordinate, Ycoordinate;
std::string coordinateColumn1, coordinateColumn2;
while (coordinates >> coordinateColumn1 >> coordinateColumn2) {
    Xcoordinate.push_back(coordinateColumn1);
    Ycoordinate.push_back(coordinateColumn2);
}


// Final output: this file can be used to plot 3 dimensional
//temperature distributions or animated gifs
for (size_t i = 0; i < board.size()/120; ++i) {
    for (int j = 0; j < 120; j++){
```

```cpp
            // Write the board entry with coordinates to the
            //outputfile file
            outputfile << Xcoordinate[j] << "\t" << Ycoordinate[j]
            << "\t" << board[i*120+j] << "\n";
        }
        outputfile << "\n";
        //gnuplot recognizes "blocks" separated
        //by two blamk lines, there is one block for
        //every sceond and we can later choose the time
        //we want to plot via an index for the block
        outputfile << "\n";
    }



// Final outputline: this is for the used for the lineplots seen
//in the thesis
for (size_t i = 0; i < board.size()/120; i++) {
    for (int j = 0; j < 120; j+=12){
        // Write the board entry with corresponding X coordinate
        //to the output_line file
        output_line << Xcoordinate[0 + j] << "\t" <<
        board[i*120+j]
    << "\t" << Xcoordinate[3 + j] << "\t" << board[i*120+j+3]
    << "\t" << Xcoordinate[6 + j] << "\t" << board[i*120+j+6] <<
    "\t" << Xcoordinate[9 + j] << "\t" << board[i*120+j+9]
    << "\n";
        output_line << Xcoordinate[1 + j] << "\t" << board[1+i*120+j]
        << "\t" << Xcoordinate[4 + j] << "\t" <<
        board[i*120+j+4]
        << "\t" << Xcoordinate[7 + j] << "\t" << board[i*120+j+7]
        << "\t" << Xcoordinate[10 + j] << "\t" << board[i*120+j+10] <<
        "\n";
        output_line << Xcoordinate[2 + j] << "\t" << board[2+i*120+j]
        << "\t" << Xcoordinate[5 + j] << "\t" << board[i*120+j+5]
        << "\t" << Xcoordinate[8 + j] << "\t" << board[i*120+j+8] << "\t"
        << Xcoordinate[11 + j] << "\t" << board[i*120+j+11]
        << "\n";

    }
```

```cpp
        output_line << "\n";
        output_line << "\n";
    }




    // Close the files
    inputfile.close();
    outputfile.close();
    output_board.close();
    output_air.close();
    output_line.close();
    coordinates.close();


    std::cout << "Successful\n";

    return 0;
}
```

References

[1] Stephen B. Pope. *Turbulent Flows*. Cambridge University Press, 2000.

[2] Kyrre Skjerdal. "Photoproduction of rho 0 in ultra–peripheral nuclear collisions at ALICE". In: *Journal of Physics: Conference Series* 455 (2013), p. 012010. ISSN: 1742-6596. DOI: 10.1088/1742-6596/455/1/012010. URL: http://dx.doi.org/10.1088/1742-6596/455/1/012010.

[3] J.C. Han and L.M. Wright. *Analytical Heat Transfer*. CRC Press, 2022. ISBN: 9781000597349. URL: https://books.google.de/books?id=fkZuEAAAQBAJ.

[4] "Letter of intent for ALICE 3: A next-generation heavy-ion experiment at the LHC". In: (Nov. 2022). arXiv: 2211.02491 [physics.ins-det].

[5] Raphaelle Bailhache. "Physics programme of the ALICE 3 experiment for the LHC Runs 5 and 6". In: *EPJ Web of Conferences* 276 (Mar. 2023). DOI: 10.1051/epjconf/202327605002.

[6] *ALICE website*. URL: https://alice-collaboration.web.cern.ch/.

[7] *Boussinesq eddy viscosity assumption*. URL: https://www.cfd-online.com/Wiki/Boussinesq_eddy_viscosity_assumption.

[8] *COMSOL Documentation: The k-epsilon turbulence model*. URL: https://doc.comsol.com/6.2/docserver/#!/com.comsol.help.cfd/cfd_ug_fluidflow_single.06.106.html.

[9] *COMSOL Documentation: Turbulence Modeling*. URL: https://doc.comsol.com/6.2/docserver/#!/com.comsol.help.cfd/cfd_ug_fluidflow_single.06.103.html.

[10] *COMSOL Multiphysics® Simulation Software*. URL: https://www.comsol.com/comsol-multiphysics.

[11] *converging-diverging nozzle*. URL: https://en.wikipedia.org/wiki/Isentropic_nozzle_flow#/media/File:20140608074127!A_converging-diverging_nozzle_with_reservoir_pressure_fixed.jpg.

[12] *Darcy-Weisbach equation*. URL: https://www.thermal-engineering.org/what-is-darcy-weisbach-equation-definition/.

[13] *Isentropic flow*. URL: https://www.grc.nasa.gov/WWW/K-12/airplane/isentrop.html.

[14] *LHC Website.* URL: https://home.cern/science/accelerators/large-hadron-collider.

[15] *Mass flow choking.* URL: https://www.grc.nasa.gov/WWW/K-12/airplane/mflchk.html.

[16] *Material properties.* URL: https://www.engineeringtoolbox.com/material-properties-t_24.html.

[17] *Moodys chart.* URL: https://en.wikipedia.org/wiki/Moody_chart#/media/File:Moody_EN.svg.

[18] *PCB documentation.* URL: http://hwstar.physi.uni-heidelberg.de/~angelov/ALICE3_SerPwr/Heat_Board/N211A1-1_heat_pcb.pdf.

[19] *Pictures from the video lecture.* URL: https://www.youtube.com/watch?v=SVYXNICeNWA&list=PLnJ8lIgfDbkrNyps1_36tNRRQ7hLzPFhV&index=1.

[20] *Specification sheet of the used fans.* URL: https://www.arctic.de/media/4a/be/ab/1699346344/Spec_Sheet_S8038-10K_DE.pdf.

[21] *The Finite Element Method (FEM).* URL: https://www.comsol.com/multiphysics/finite-element-method.

Eigenständigkeitserklärung

Ich versichere, dass ich diese Arbeit selbstständig verfasst und keine anderen als die angegebenen Quellen und Hilfsmittel benutzt habe.

Heidelberg, den 05.03.2024

Henry Rainer

Acknowledgement